CRYSTAL GROWTH & DESIGN

pubs.acs.org/crystal Article

Lithium Functionalization Promoted by Amide-Containing Ligands of a Cu(*pzdc*)(*pia*) Porous Coordination Polymer for CO_2 Adsorption Enhancement

Karina Riascos-Rodríguez, Samuel Marks, Paul G. Evans, Samuel P. Hernández-Rivera, Jose L. Ruiz-Caballero, Dalice Piñero, and Arturo J. Hernández-Maldonado*

Cite This: *Cryst. Growth Des.* 2020, 20, 3898−3912 Read Online

ACCESS | Metrics & More | Article Recommendations | Supporting Information

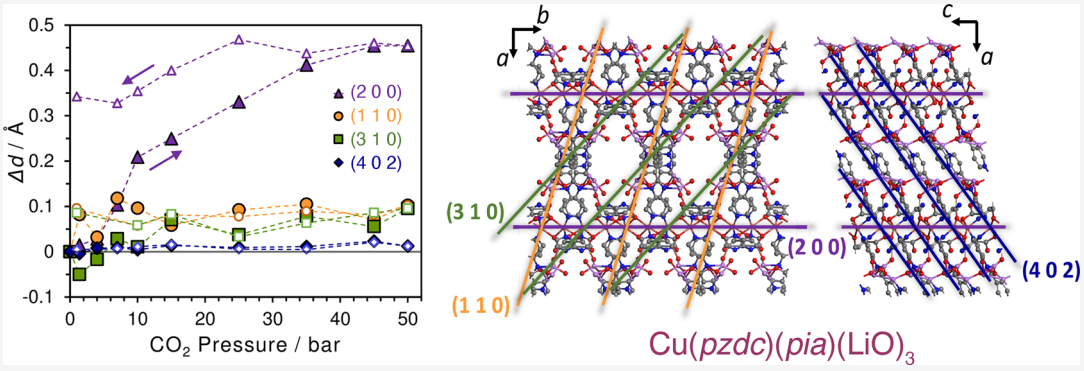

ABSTRACT: A pillared layer network containing amide functional groups (Cu(*pzdc*)(*pia*); *pzdc* = pyrazine-2,3-dicarboxylate; *pia* = *N*-(4-pyridyl)isonicotinamide) was used to test a postsynthesis metalation rationale to insert lithium and create a porous surface with enhanced CO_2 adsorption capacity. Synchrotron powder X-ray diffraction (XRD) was used to determine variations after lithiation in long-range and textural properties. CO_2 adsorption measurements at room temperature showed a concave up isotherm shape with an increasing adsorption at high pressures, surpassing by 1 order of magnitude the values previously reported for the unmodified material. There was significant hysteresis upon desorption, which suggests structural variations consequent to different or stronger adsorption sites. Results from elemental, thermal gravimetric, and crystal refinement analyses indicate that the lithium content is ca. 3 Li atoms per asymmetric unit. Raman scattering showed N−Li and Li−O stretching bands, a shift of *pia* amide- and pyridyl-related bands, and other significant skeletal vibrations associated with nitrogen and oxygen lone pair variations. *In situ* XRD and CO_2 adsorption observations at up to 50 bar at ambient temperature were consistent with the anticipated structural dynamic variation. The lattice changes observed at pressures below 10 bar following lithiation may be directly related to an enhancement in the CO_2 adsorption amount.

1. INTRODUCTION

CO_2 emissions from fossil fuel burning remain a concern; values reached an unprecedented level of about 36 billion tons in 2016.[1,2] Traditional amine sorbents are usually employed to treat flue gases prior to emission under specific and constant operation conditions, but at the expense of high energy input for regeneration and operational and practical problems that include corrosion and toxicity.[3,4] Porous coordination polymers (PCPs) or metal−organic frameworks (MOFs) present an alternative direction toward the development of next-generation materials for CO_2 capture or separation at the emission point. PCPs exhibit properties that can be tailored to specific gas uptake requirements. These properties can be manipulated *a priori* through the rational selection of the factors that dictate the assembly route during synthesis or *a posteriori* through functionalization strategies.[5,6] For CO_2 adsorption applications, a group of pillared layer networks, i.e., $[Cu^{2+}_x(pzdc)_y(L)_z]_n$ (*pzdc* = pyrazine-2,3-dicarboxylate; *L* = ditopic ligand)[7−12] have been of interest due to their potential gas storage and separation capabilities and their stability at low to medium pressures, e.g., up to 6 atm at ambient temperature, broadening the pressure scope to design or optimize processes for CO_2 adsorption.[13−18] Although adsorption and desorption equilibrium tests exhibit a hysteretic

Received: February 17, 2020
Revised: April 29, 2020
Published: April 30, 2020

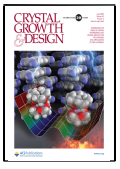

https://dx.doi.org/10.1021/acs.cgd.0c00202
Cryst. Growth Des. 2020, 20, 3898−3912

behavior that varies according to the highest gas pressure attained before desorption, there is evidence of a structural response without degradation of the long-range periodicity and porosity.[15,16] $Cu^{2+}_x(pzdc)_y(L)_z$ materials have favorable attributes, including one-pot crystallization under ambient conditions and conformation of one-dimensional channels with ligands that can accommodate functional groups along the pores. There is thus a strong motivation to upgrade the internal surface of PCPs or MOFs through chemical functionalization.

The insertion of alkali or alkaline-earth metals onto adsorbate-accessible sites along the pores of a crystalline material can enhance the surface polarizability, which calculations predict to be a key property in the adsorbate−adsorbent interaction potential.[19,20] The polarizability and low atomic weight and size of Li could allow for the adjustment of the adsorbate−adsorbent interactions, without significantly diminishing the pore volume or causing a steric reduction in the capacity for mass transport along the pores. A metalation approach, i.e., lithium incorporation, could enhance the CO_2 uptake capacity of PCPs. Lithiation strategies for the functionalization of porous nets arranged through stable coordination bonds are of interest, since the preservation of the framework is essential when the metal atom is incorporated.[21,22] A postsynthesis metalation to change intramolecular modifications is achievable by incorporating a ligand with primary and secondary donor sites, in which the primary site is coordinated to conform the framework structure and the secondary site remains available for postsynthesis modifications. This configuration can also be attained by the choice of framework ligands and the metal center according to the hard−soft acid−base theory to leave uncoordinated sites available for functionalization.[5,21,23,24]

There have been some reports that modifying the surface chemistry of the pores with specific moieties leads to increased CO_2 adsorption capacities, such as in the case of a MOF series of SIFSIX pillared nets.[25−27] Another example is the case of MOF-74-Mg, a framework featuring an alkaline-earth metal as the central node, evidencing open metal sites (OMS) and conforming one-dimensional porous channels. This material adsorbed 8 mmol of CO_2 g^{-1} at 296 K and 1 bar (or ca. 12 CO_2 molecules per unit cell), among the highest uptake amounts for MOFs under such conditions.[6,28,29] However, the CO_2 uptake of MOF-74-Mg was reduced by the presence of humidity, which is typically present in flue gas applications such as power plants. Amines and alkylamines have been added to the OMS, which leads to proper performance under humid conditions but likely under a chemisorption regime.[30−32]

There is still no consensus on the possible effects of size and chemical properties of groups incorporated into PCPs or MOFs. While some studies suggest structural or flexibility changes,[5,33−37] there remains much work to be done to establish direct correlations. Much of the effort in the case of alkali- and alkaline-earth-metal incorporation has focused on hydrogen storage[33,38−44] and on the improvement of CO_2 adsorption or selectivity in gas mixtures.[34,35,37,45−56] Theoretical and experimental studies have been conducted to study Li incorporation into frameworks with Zn metal centers[33−35,39−42,45−47,50,53,54,57] and other metal nodes, including Cu, Zr, Cr, Al, and In.[37,38,40,43,44,48,49,51,52] Simulations have explored frameworks with (1) substitution of one or more selected hydrogen atoms of the aromatic rings by Li or LiO or (2) Li added to positions apparently prone to accept cations or estimated as less energetically demanding: e.g., above or on top of the electron clouds of the aromatic rings.[34,35,37,40−42,44−46,48,50,51,53,57] Similarly, experimental results show that Li has been inserted through the exchange of hydrogen from hydroxy groups, pore guests, or even nodes and the doping of carboxyl groups or their incorporation as a cation, which in some cases resulted in sensitivity to air exposure or retraction to unexposed adsorption sites.[33,38,39,43,47,49,52,54] The observed gas uptake enhancements were moderate in comparison to the targets predicted by computational studies, in some cases ascribed to diminishments in the isosteric heat of adsorption with pressure, effects of the free pore volume, and transport characteristics.[40,52]

In this work, a lithium alkoxide precursor (i.e., LiO-*t*-Bu) was used to functionalize a pillared layer porous coordination polymer, Cu(*pzdc*)(*pia*) (*pzdc* = pyrazine-2,3-dicarboxylate; *pia* = *N*-(4-pyridyl)isonicotinamide), in which the *pia* ligands could play a role in guiding the incorporation of lithium into the framework: i.e., lithiation through an amide directing metalation group (DMG) (see Figure 1). The structures were

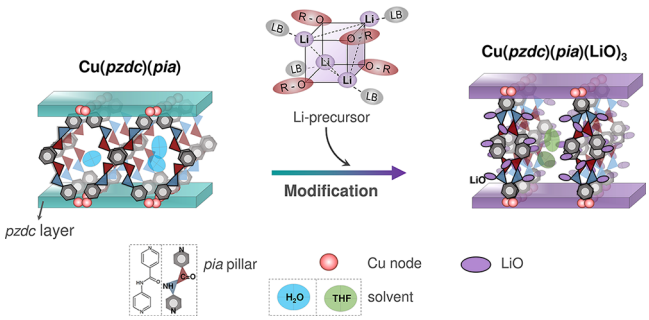

Figure 1. Schematic representation for the structural conformation of a lithiated Cu(*pzdc*)(*pia*) PCP. The Li precursor shown is a representation of aggregates of LiO-*t*-Bu in THF, which comprises a Lewis base (LB) and an alkyl group (R = *tert*-butyl).

studied using synchrotron X-ray powder diffraction (XRD). Rietveld refinement results were consistent with a porous-pillared-layer lattice configuration and were consistent with the structural changes expected to result from functionalization. The incorporation of the Li ions was also probed by elemental and thermal gravimetric analyses (TGA). Comparisons of Raman scattering changes in intensity or band peak positions indicated the effects of the amide DMG on the functionalization approach. These observations offered crucial insights into the transformations observed in the CO_2 adsorption−desorption isotherms measured up to 7 bar at ambient temperature and the hysteretic behavior for the lithiated material. The lithiation-related structural variations upon CO_2 adsorption were also apparent in *in situ* powder X-ray diffraction measurements with CO_2 gas pressurization−depressurization cycles at up to 50 bar at ambient temperature. An isoreticular framework counterpart, $Cu_2(pzdc)_2(dpyg)$ (*dpyg* = 1,2-bis(4-pyridyl)glycol), was also studied as a control experiment isolating the effect of the absence of the amide group on the effects of lithiation on CO_2 adsorption and the structural response.

2. EXPERIMENTAL SECTION

2.1. Reagents and Materials. 2,3-Pyrazinedicarboxylic acid (H_2pzdc, 97%), copper(II) perchlorate hexahydrate ($Cu(ClO_4)_2 \cdot 6H_2O$, 98%), denatured ethanol (95%), and methanol (99%) were

https://dx.doi.org/10.1021/acs.cgd.0c00202
Cryst. Growth Des. 2020, 20, 3898−3912

used for the synthesis steps. The functionalization was conducted using lithium *tert*-butoxide (LiO-*t*-Bu, 97%) and tetrahydrofuran (99.9%). The hydroxy-based pillar ligand 1,2-bis(4-pyridyl)glycol (*dpyg*) and the other synthesis and functionalization reagents were obtained from Sigma-Aldrich and used as received, except for the amide-based pillar ligand *N*-(4-pyridyl)isonicotinamide (*pia*, 97%), which was acquired from MolPort. Ultrahigh-purity-grade He and N_2 gases used for the TGA measurements were obtained from Praxair. Ultrahigh-purity-grade CO_2 gas was employed for the gas adsorption isotherm measurements, as supplied by Praxair. Ultrahigh-purity-grade CO_2 and N_2 compressed gases used for the *in situ* XRD experiments were obtained from AirGas and used without further treatment.

2.2. Cu(*pzdc*)(*pia*) and Cu_2(*pzdc*)$_2$(*dpyg*) Syntheses. Cu(*pzdc*)(*pia*) and Cu_2(*pzdc*)$_2$(*dpyg*) were prepared following routes reported elsewhere.[8,9,13,14] A mixture of a 0.04 M NaOH solution and ethanol prepared in a 1:1 ratio was used to dissolve 1 mmol of H_2pzdc (0.1681 g) and 0.5 mmol of the pillar: (a) *pia* (0.0995 g) for Cu(*pzdc*)(*pia*) or (b) *dpyg* (0.1171 g) for Cu_2(*pzdc*)$_2$(*dpyg*). Separately, another mixture composed of $CuClO_4{\cdot}6H_2O$ (0.3705 g) and water was kept under strong and continuous agitation while the initial reaction mixture was added dropwise. This step generated an opaque light blue suspension that was kept under agitation for 24 h and then was vacuum-filtered and repeatedly washed with methanol and deionized water. The recovered solid was partially dried to remove excess water or solvent, in a conventional oven at 363 K for 24 h. The final solid sample was maintained in a vacuum-sealed desiccator until further use.

2.3. Postsynthesis Lithium Incorporation. The functionalization procedure presented here is based on chemical insight into metalation derived from the heterocycle chemistry literature, including into the formation of lithiated amides and into experimental assays for the characterization of alkoxide functionalization in MOFs.[5,36,39] A room-temperature procedure involving tetrahydrofuran (THF) was chosen (i) to investigate the lithiation that is thermodynamically favored under the particular conditions, (ii) to keep a low aggregation number for the lithium source, and (iii) to preserve the coordination stability of the parent framework. In order to conduct the synthesis safely, the whole lithiation procedure was carried out inside a controlled, dry atmosphere glovebox. A portion of the dry powder sample recovered at the end of the synthesis stage (~100 mg) was combined with excess THF to form a suspension that was vacuum-filtered several times with fresh solvent. Afterward, the PCP was kept soaking in THF for at least 12 h at room temperature. Once ready, the sample was rewashed and left in fresh solvent (50 mL) with continuous vigorous stirring. Separately, 0.68 mmol of LiO-*t*-Bu in a solution at least 0.01 M in THF was prepared and stirred vigorously until a clear, noncloudy pale liquor was obtained. This liquor was kept under continuous agitation while it was added dropwise to the PCP framework suspension. During this stage, the initially pale blue opaque suspension turned turquoise. It should be noted that a large lithium content can turn a suspension dark gray within the first 1 h of mixing and the strong base could lead to a PCP framework decomposition. After 24 h of agitation, the final suspension was filtered under vacuum, washed with THF, and left to slowly dry at room temperature inside a dry chamber before it was stored in a vacuum-sealed desiccator for further analysis stages.

2.4. Thermogravimetric and Metal Content Analyses. TGA was used to determine the solvent content and to identify variations in the thermal degradation pathway of PCPs as a consequence of lithiation. A thermogravimetric analyzer (TA-Q500) with a platinum sample pan was employed for the thermal analyses. Each sample before lithiation (~8 mg) was heated from room temperature to 1173 K at 5 K min^{-1} under a constant helium flow rate (60 mL min^{-1}). In the case of the Li-containing samples, the heating programming included a 4 h soaking stage after the temperature reached 1073 K. The soaking stage was necessary to fully record the ultimate weight loss. The Li and Cu contents of the PCPs were evaluated via inductively coupled plasma mass spectroscopy (ICP-MS) at Galbraith Laboratories Inc.

2.5. Synchrotron Powder X-ray Diffraction. Synchrotron source powder X-ray diffraction patterns for as-synthesized Cu(*pzdc*)(*pia*) and Cu_2(*pzdc*)$_2$(*dpyg*) were recorded before and after lithiation at the National Synchrotron Light Source II (NSLS-II) at Brookhaven National Laboratory. Each sample was packed into a polyimide capillary and probed using an X-ray wavelength of 0.183893 Å, corresponding to a photon energy of 67 keV. The diffracted intensity was collected using 60 s exposure times with an area detector covering a 2θ angular range from 0.03 to 176°. The GSAS II software package was used to perform the initial data integration, to determine the initial instrument parameters with a Ni standard data set, and to conduct indexing, structureless Pawley analysis, and Rietveld refinement.[58] The 2θ range before and after lithiation used for fitting and pseudo-Voigt peak shape modeling comprised diffraction intensities collected from 0.5 to 10°. This 2θ range covered the most intense reflections. The fitting of the background scattering before and after functionalization was carried out using 30- and 18-term Chebyshev expressions, respectively. The structure was solved on the basis of preliminary results from the *ab initio* charge-flipping tool also available in GSAS II and the variation of the orientation, position, and conformation of an asymmetric unit constructed with the guidance of crystalline structures of other Cu-based pillared layer networks, the crystal structures of the parent organic ligands, and the octahedrally Cu^{2+} coordinated node. These angles and atomic bond distances were intrinsically restrained.

2.6. Adsorption/Desorption Measurements. CO_2 adsorption and desorption equilibrium isotherms covering low- and high-pressure ranges were volumetrically measured at 25 °C, employing Micromeritics ASAP 2020 and 2050 adsorption analyzers, respectively. High-pressure volumetric discrepancies were accounted for by using compressibility factor corrections in the calculations of the uptake amount. Each PCP sample had a mass of approximately 100 mg, carefully introduced into a quartz flask or a stainless-steel tube for the high-pressure tests. Immediately after loading, the vessels were capped using seal frits designed to achieve a valvelike interconnection with the analysis port and to shield the samples from the external ambient atmosphere. An initial activation step was performed to prepare the sample before the adsorption stage through the removal of solvent or contaminant molecules weakly attached to the pores. The sample was activated by evacuating the sample holders at a rate of 50 mmHg s^{-1} until a final pressure of 5 mmHg was reached. The sample was heated under vacuum at a ramp rate of 10 K min^{-1} to 373 K and held at that temperature for at least 12 h. After this activation process was complete, the sample was cooled to ambient temperature under vacuum. The sample holder was backfilled with helium to facilitate the sample relocation to the adsorption analysis port without exposure to the atmosphere. The gas used for backfilling was evacuated using the analysis port before the programmed adsorption cycle. The instrument adsorption/desorption equilibration time interval used was 100 s, which allowed collection of transient data for at least 1100 s during the assessment of equilibrium conditions.

Heats of desorption profiles for CO_2 loading onto lithiated Cu(*pzdc*)(*pia*) or Cu_2(*pzdc*)$_2$(*dpyg*) materials were estimated using the expression[59]

$$-\Delta H = \Delta H_{vap} + \beta_{DA}E\left(\ln\frac{q_0}{q}\right)^{1/n} + \frac{(\beta_{DA}E)\delta T}{n}\left(\ln\frac{q_0}{q}\right)^{-\left(\frac{n-1}{n}\right)} \quad (1)$$

which results after combination of the Dubinin–Astakhov isotherm model (applied to the desorption legs)

$$q = q_0 \exp[-(C\ln(P_o/P))^n] \quad (2)$$

$$C = \frac{RT}{\beta_{DA}E}$$

and the Clausius–Clapeyron equation

https://dx.doi.org/10.1021/acs.cgd.0c00202
Cryst. Growth Des. 2020, 20, 3898−3912

$$-\Delta H = R\frac{\mathrm{d}\ln P}{\mathrm{d}(1/T)}\bigg|_{@\text{constant loading}} \quad (3)$$

where ΔH_{vap} is the adsorbate heat of vaporization, q is the equilibrium desorption amount, q_0 is the adsorbate loading amount at or near saturation, T is the temperature during the desorption tests, β is the affinity coefficient of the adsorbate, E is the energy of desorption, P is the gas pressure, P_o is the adsorbate vapor pressure, n is a heterogeneity coefficient, δ is a thermal expansion coefficient for the adsorbate (assumed as 0.0024 K^{-1}),[60] and R is the ideal gas constant.

2.7. *In Situ* CO_2 or N_2 Adsorption and Powder X-ray Diffraction. The evolution of the X-ray diffractograms measured as a function of CO_2 or N_2 gas pressure was recorded *in situ* for as-synthesized Cu(*pzdc*)(*pia*) and Cu_2(*pzdc*)$_2$(*dpyg*), before and after lithiation, by using a gas supply system integrated with a laboratory diffractometer. The sample holder consisted of a 1.2 mm diameter polyimide capillary. The powder was loaded into the capillary and connected to a stainless-steel gas delivery system providing CO_2 or N_2. The diffraction data were acquired using Cu Kα radiation with a wavelength of 1.5406 Å from a Rigaku Ultra-X 18 rotating anode X-ray generator operating at 40 kV and 100 mA. The sample was activated before the diffraction experiment in a continuous flow of pure N_2 to remove solvent and impurities from the pores. The sample holder was heated to the activation temperature of 373 K using a hot air stream at a heating rate of 20 K min^{-1} and kept at this temperature for at least 1 h. The N_2 flow was interrupted only after the sample reached ambient temperature after the end of the heating process. The inlet and outlet gas valves were simultaneously closed after the end of the activation process. The gas environment was chosen as CO_2 or N_2 to start the experiment, and the corresponding gas was delivered to the sample holder until the targeted working pressure was reached (up to ca. 50 and 15 bar for CO_2 and N_2, respectively). The diffraction patterns were recorded for 2θ values from 4 to 30° before and after the activation and for each target pressure.

2.8. Raman Spectroscopy. Raman spectroscopy was employed to characterize as-synthesized Cu(*pzdc*)(*pia*) and Cu_2(*pzdc*)$_2$(*dpyg*) before and after lithiation. Raman spectra were recorded at room temperature using an InVia Renishaw microspectrometer with a 785 nm laser. The calibration of the laser was conducted using a Si (100) standard. The spectrum range was covered from 100 to 3200 cm^{-1}, using an integration time of 120 s and five accumulations. The powder sample was mounted on a gold plate and probed with a Leica microscope equipped with a 50× objective. A Savitzky and Golay least-squares digital polynomial filter was used to smooth the spectrograms after regressing and removing the background signal.

3. RESULTS AND DISCUSSION

3.1. Effect of Lithiation on the Cu(*pzdc*)(*pia*) Structure and Thermal Stability. The structures of the PCPs under study in this work were elucidated via modification of the lattice of isoreticular neutral three-dimensional pillared-layer networks; similar structures have been reported and discussed elsewhere.[8,11−13,61] Here, the *pia* bidentate pillar ligand contains a central nonsymmetrical amide functionality that could affect the basicity of each pyridyl nitrogen donor dent and promote a bias in the coordination to Cu. The Cu−ligand bonding could thus possibly occur only at one dent of the ligand backbone. Such a configuration was previously reported for an homologous PCP ($[Cu(pzdc)(pia)_2]_n$) that was synthesized with a methanol solution instead of ethanol.[62]

The crystal lattice of the as-synthesized PCPs (i.e., before and after lithiation with sorbed solvent) was determined using Rietveld analysis of the synchrotron powder diffraction data. Figure 2 shows the synchrotron powder X-ray diffraction patterns of the as-synthesized nonlithiated and lithiated materials. The pillared-layer conformation that was determined

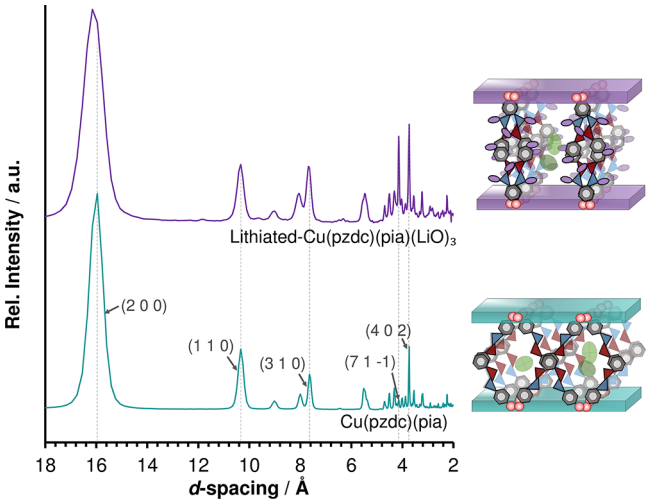

Figure 2. Synchrotron powder X-ray diffraction patterns for as-synthesized Cu(*pzdc*)(*pia*) and Cu(*pzdc*)(*pia*)$(LiO)_3$, both containing sorbed H_2O and THF (i.e., solvents), respectively.

from the Rietveld refinement analysis is shown in Figure 3. As is apparent, for the porous channels the key structural changes induced by the Li precursor are a change in the orientation of the pillars and the addition of LiO at sites near *pia* pillar ligands.

Further structural details are illustrated in Figure 3. The octahedrally coordinated Cu centers are interconnected by *pzdc* ligands that fill the equatorial positions in a configuration that chelates the metal ions. The pillars form nets with the similar orientation into two-dimensional layers. The axially oriented coordination positions of each Cu-containing layer are filled at one end by *pia* ligands, which self-arrange to share nonbonding aromatic π-stacking interactions with *pia* linkers from neighboring layers. These nonbonding interactions stabilize a parallel alignment of the layers that results in the formation of porous channels with self-rearrangement capabilities. For instance, the pore channel contents, such as solvent molecules, can induce key changes in the orientation of the ligands by hydrogen bonding and weak cooperative effects.

The results of the Rietveld refinement and corresponding reliability factors are given in Table 1 and illustrated in Figure S-1 in the Supporting Information. The most important structural features of the original framework are retained after lithiation. Similarly, the most intense X-ray reflections, those related to the spacings of the backbone of the frameworks, are observed in the X-ray diffraction patterns of both materials in Figure 2. The similarity of the diffraction patterns acquired before and after lithiation provided the starting point for the determination of the structure of the lithiated framework. This initial structure guided the determination of the location of the Cu atoms but provided less insight into the positions of Li and other light atoms. Raman spectroscopy results, which are discussed in detail in the section 3.2, gave insight into the Li moiety (i.e., LiO) location. Mesomeric effects, inductive effects and nonbonding interactions that lead to disorder, also served to explain the position of the Li moiety near the *pia* pillar ligands. Crystallographic results for the lithiated framework indicated that Cu atoms have a distorted coordination geometry in which the pillar positions are displaced. These two effects also suggested a complementary reorientation of the pyrazine rings from axial to equatorial, as illustrated in

https://dx.doi.org/10.1021/acs.cgd.0c00202
Cryst. Growth Des. 2020, 20, 3898−3912

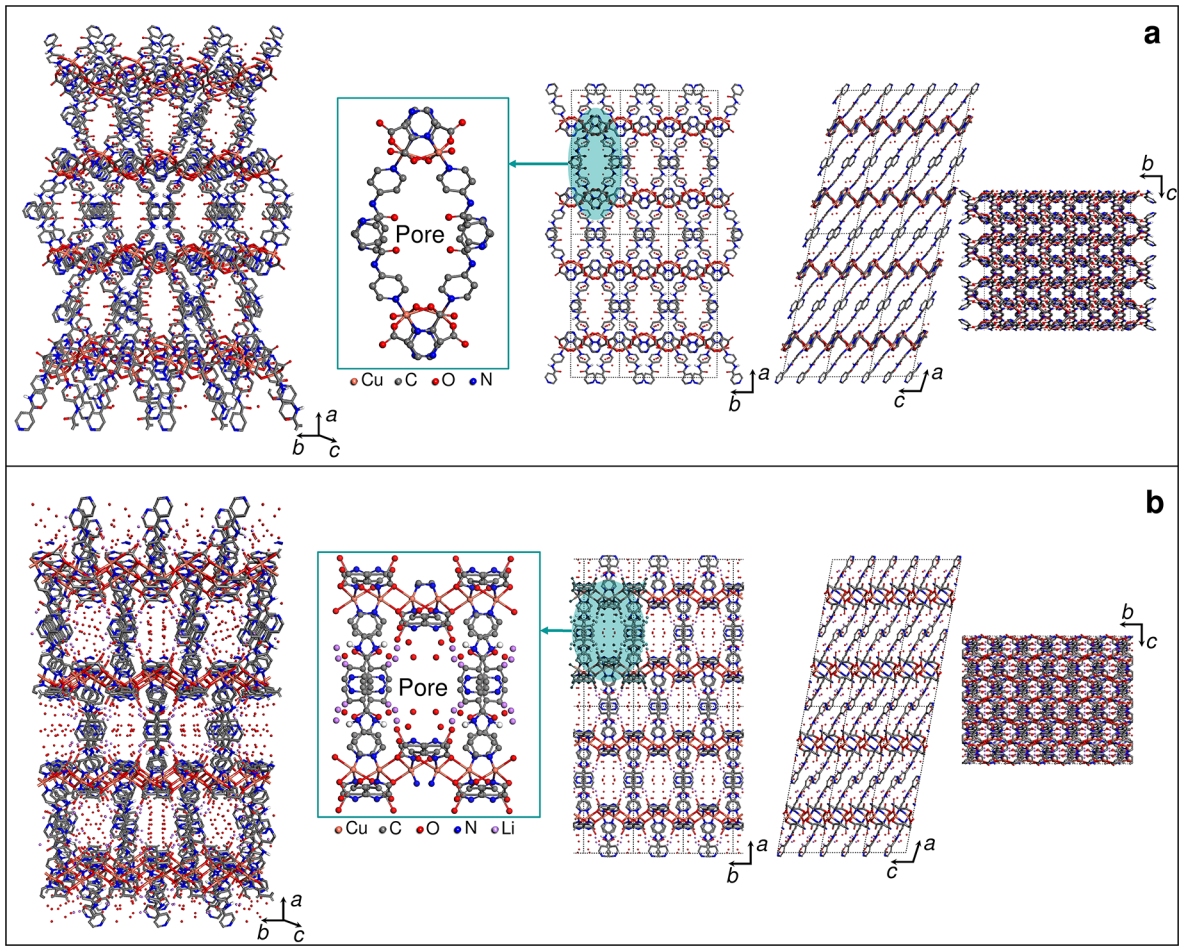

Figure 3. Rietveld refinement structural models for (a) Cu(*pzdc*)(*pia*) and (b) Cu(*pzdc*)(*pia*)$(LiO)_3$. The insets shown in (a) and (b) are amplified views of the pore channels of each framework. Hydrogen atoms are omitted for clarity.

Figure 3. The pyrazine ring reorientation is consistent with the change in color of the powder sample due to the functionalization stage. ORTEP drawings with 30% probability ellipsoids are available in Figure S-2 in the Supporting Information.[63]

The crystalline structure of the lithium *tert*-butoxide (LiO-*t*-Bu) precursor has a folded hexameric or octameric aggregated configuration.[64] The X-ray diffraction patterns and the crystallographic results in Figures 2 and 3 and in Table 1 show no sign that the bulky organic portion of the lithiation precursor is incorporated into the final structure. At the lithiation stage, the LiO-*t*-Bu crystals were initially dissolved in THF, which has been reported to lead to aggregation in tetramers.[65−67] Solvation can produce the THF heterocycle ring aperture through weak interactions originating in the oxygen π-orbital electron delocalization toward the lithium nuclei. A tetrameric alkoxide configuration with four Li−O−Li−O squares in which the *tert*-butyl units flank out bonded to the oxygen corners could stabilize the Li−O bonds through inductive effects. During lithiation, interactions of the alkoxide aggregates with the framework possibly promoted a further unfolding of the lithium tetramers to a more fragmented configuration, facilitating the incorporation of Li−O and impeding the attachment of bulky *tert*-butyl segments. This "selective softness" could be explained by a combined influence of steric and collective effects from the nonbonded free pyridyl nitrogen site in the *pia* and the amide, pyrazyl, and pyridyl conjugate systems, although further investigations are needed to confirm this hypothesis. Neutral ligands may fulfill the lithium coordination sites produced by the unfolding of the aggregates. The free electron pair donors from the framework and solvents such as THF and THF cleavage derivatives can bind to lithium through a neutral−neutral connectivity. Similar connections can take place with any other charge-complementary ligand small that is enough to move into the pore cavities.

Because of its low atomic number, Li makes a negligible contribution to the distribution of X-ray intensity in a diffraction pattern. For the structural model, the Li−O had initial interatomic distances similar to those reported elsewhere for the octameric and hexameric aggregates. The location of LiO in the backbone of the framework was established from the Raman spectroscopy results that are discussed in section 3.2. Thus, the positions of Li and surrounding atoms were adjusted by refinement, and the resulting positions were kept in the structural model as shown in Figure 3b.

The thermal stability of the lithiated framework and the possible chemical effects of the functionalization were studied using TGA. The decomposition profiles for the materials before and after lithiation are shown in Figure 4. The profiles were used to indirectly analyze chemical variations, considering that under limited constraints the decomposition of the lithiated framework could follow paths similar to those of the framework before lithiation and of other isoreticular Cu-

https://dx.doi.org/10.1021/acs.cgd.0c00202
Cryst. Growth Des. 2020, 20, 3898−3912

Table 1. Unit Cell Parameters and Rietveld Refinement Reliability Factors for as-Synthesized Cu(*pzdc*)(*pia*) and Cu(*pzdc*)(*pia*)$(LiO)_3$, Including Sorbed Solvents

	Cu(*pzdc*)(*pia*)⊃H_2O	Cu(*pzdc*)(*pia*)$(LiO)_3$⊃THF
empirical formula	$C_{17}H_{11}CuN_5O_9$	$C_{17}H_{11}CuLi_3N_5O_{11}$
formula wt	492.85	545.67
T (K)	300	300
cryst syst	monoclinic	monoclinic
space group	$C2/c$	$C2/c$
a (Å)	32.73(3)	32.80(3)
b (Å)	10.910(5)	10.926(5)
c Å)	9.682(3)	9.441(3)
β (deg)	102.131	100.716
volume (Å^3)	3380(4)	3324(4)
Z	8	8
R_p	0.0783	0.0494
R_{wp}	0.1172	0.0704
R_{exp}	0.2225	0.2379
$R(F^2)$	0.1704	0.1796
$R(F)$	0.0707	0.0802
no. of rflns	1499	1482
instrument	synchrotron	synchrotron
χ^2	338.005	106.102
GOF	0.53	0.3
χ_ν^2	0.2809	0.09

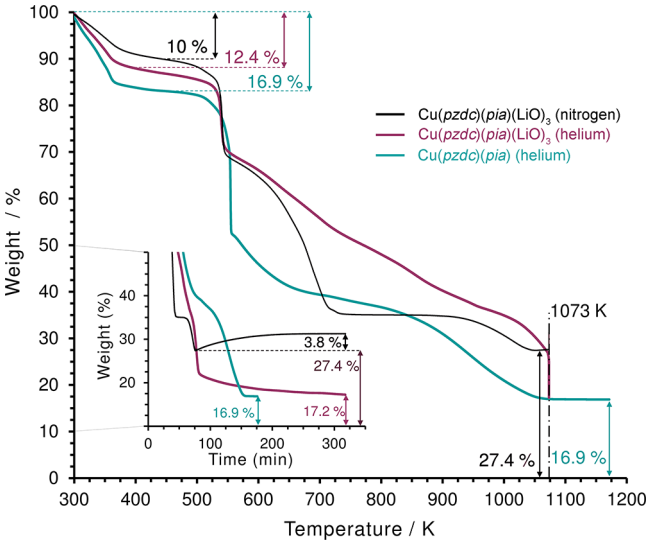

Figure 4. Thermal gravimetric profiles of Cu(*pzdc*)(*pia*) and Cu(*pzdc*)(*pia*)$(LiO)_3$ under either helium or nitrogen gas.

pillared layer networks.[14,15] The profile of the lithiated framework in helium carrier gas exhibits decomposition starting at 433 K, followed by an abrupt weight loss of 19.4 wt % at 540 K that is associated with structural decomposition and also involves losses of organic segments from *pzdc* and *pia* ligands (second and third losses: ca. 51.5 wt %). At lower temperatures, the mass loss of 12.4 wt % arises from solvent molecules that are weakly attracted to the pores and outer surfaces of the crystallites. A loss that probably tracks oxygen, nitrogen, and carbon traces that reacted or formed an adduct with lithium during the thermal analysis generates a less active weight loss (fourth loss: 13.9 wt %).

In a final stage, the TGA in helium was prolonged to 4 h at 1073 K with a loss of 5 wt % until no further mass loss was discernible, leaving a remnant solid with 17.2 wt % of the initial solid. The remnant solid is presumably composed of copper and lithium oxides. The decomposition profile, including the extended final stage, was also recorded under nitrogen. In comparison with the typical mass low rate of decomposition observed at temperatures over 750 K for the unmodified framework (Figure S-4 in the Supporting Information), the lithiated compound in nitrogen showed an unusual mass gain that reached stabilization. The incremental weight loss only concerning the lithiated sample could be explained by a reaction between a lithium oxide evolving at early stages of the TGA and the carrier gas. The TGA profiles gathered in helium and nitrogen were similar to those recorded for another pillared layer, $Cu_2(pzdc)_2(dpyg)$ (i.e., network holding *dpyg* pillars with hydroxide functionalities),[15] before and after the same lithiation approach (Figures S-3–S-5).

The TGA of the lithiated sample under helium exhibited decomposition of the organic components that extended to a higher temperature, possibly indicating the influence of new intermolecular interactions. In a previous study, a LiO-*t*-Bu TGA that was performed under nitrogen showed a single mass loss (~97%) starting at 393 K, in which 90% was lost between 498 and 548 K.[68] In another report for this alkoxide, sublimation occurred without decomposition between 443 and 478 K at 1.01 bar.[65] The absence of a larger mass loss in a TGA profile gathered under helium that is probably related to sublimation also suggests a lack of physically mixed LiO-*t*-Bu crystals.

The TGA profiles also allow the Li content of the lithiated compound to be estimated. The mass loss starting at 973 K and the distinctive mass loss corresponding to the final isothermal step at 1073 K are not observed for the framework before lithiation or similar pillared networks reported in the literature. The new features indicate that there is an inorganic-based Li–O alkoxide moiety in the framework. The TGA mass gain reported for the lithiated framework under nitrogen (Figure 4; mass gain ca. 3.8 wt % at 1073 K) was used to estimate an approximate lithium content in the solid, assuming a hypothetical reaction kinetically favored under conditions similar to those of the final isothermal TGA stage and similar to those reported elsewhere, following a global stoichiometry of $2Li(s):1N_2(g)$ between a lithium adduct or oxide and nitrogen.[69–72] Using this approximation, the lithium content was found to be ca. 3.76 wt %. Furthermore, the cell lattice previously elucidated in the crystallographic studies was used to substantiate the lithium content, Li 3.72 wt %, as well as the framework building block weight compositions (wt %): THF, 11.42; *pzdc*, 29.62; *pia*, 35.33; LiO, 12.29, Cu, 11.34 (elemental analysis: Li 3.19 wt %and Cu 14.6 wt %).

3.2. Raman Spectroscopy and Long-Range Functionalization Evidence. Figure 5 shows Raman spectra recorded for as-synthesized PCPs before and after lithiation. While both spectra exhibit many similar features, several uneven band peak displacements and relative intensity variations are discernible. The band at 149.8 cm^{-1} and other minor low-frequency bands were weaker after lithiation, indicating the influence of porous steric restrictions and weak crystal long-range nonbonding interactions that arise due to the change of solvent from water to THF. As a result, the hindrance of THF librations and the changes in the external modes could also explain the appearance of a ring-breathing vibration at 914.8 cm^{-1}.

https://dx.doi.org/10.1021/acs.cgd.0c00202
Cryst. Growth Des. 2020, 20, 3898–3912

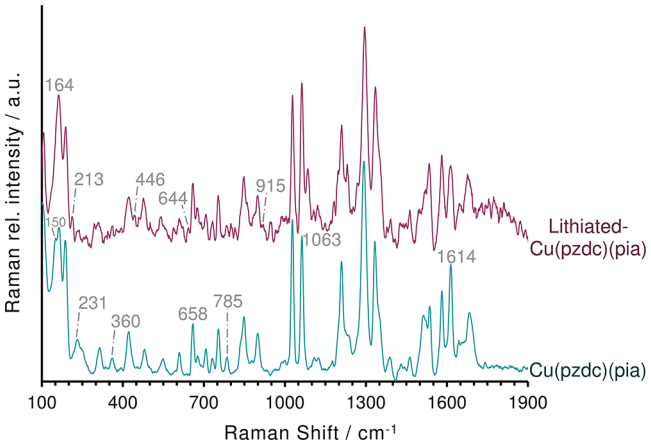

Figure 5. Room-temperature Raman scattering spectra for as-synthesized Cu(*pzdc*)(*pia*) and Cu(*pzdc*)(*pia*)$(LiO)_3$, both containing sorbed H_2O and THF (i.e., solvents), respectively.

The bands that appreciably shifted with lithiation are shown in Table 2, indicating not only symmetry similarities but also structural modifications such as those observed in the crystallographic results. These Raman shifts can guide the explanation of bonding alterations in the ligands or around the metal node produced by the incorporation of lithium. Raman bands of crystals of the building blocks of the PCP or assemblies for M−ligand pairs (M = Cu, Li) available elsewhere were used to make band peak assignments.[73−81]

Table 2. Raman Peak Interpretation and Estimated Differences of Homologous Bands for Cu(*pzdc*)(*pia*) and Cu(*pzdc*)(*pia*)$(LiO)_3$, Containing Sorbed H_2O and THF (i.e., Solvents), Respectively[a]

obsd Raman peak position, R (cm^{-1})						
Cu(*pzdc*)(*pia*)		Cu(*pzdc*)(*pia*)$(LiO)_3$		Raman variation (cm^{-1})		
				$\Delta\omega$	shift	interpretation of vibration contributions
102.2	vs	104.9	vs	2.7	blue	CuO, CuN in-plane bending-equatorial
165.6	vs	164.3	vs	−1.3	red	CuN bending tilt deformation-axial
314.6	m	309.5	m	−5.1	red	CuO, CuN stretching-equatorial
421.1	m	422.4	m	1.3	blue	CuO, CuN stretching-equatorial
482.4	m	474.9	m	−7.5	red	pyridyl out of plane ring deformation
551.5	m	541.7	m	−9.8	red	amide O=C−N bending
677.7	m	675.3	m	−2.4	red	pyridyl CC stretching and pyrazine ring deformation
706.4	m	708.8	m	2.4	blue	amide NH out of plane deformation
1124.3	w	1121.0	w	−3.3	red	pyrazine ring CC and CN stretching
1293.8	vs	1296.0	vs	2.1	blue	pyridyl CC, CN stretching, and CH bending
1613.9	s	1609.8	s	−4.0	red	pyridyl CC and CN stretching amide NH uneven deformation
1684.6	s	1679.6	s	−4.9	red	amide CO stretching

[a]Peak intensity: vs, very strong; s, strong; m, medium; w, weak. $\Delta\omega = \omega_{lithiated} - \omega_{initial}$.

The shifts given in Table 2 correspond to band peak displacements to lower or higher frequencies relatable to chemical variations, with reference to the original framework (i.e., spectrum for Cu(*pzdc*)(*pia*) shown in Figure 5). For instance, the shift of the amide O=C−N bending vibrations ($\Delta\omega$ = −9.8 cm^{-1}) could depend on the disturbance of the nitrogen lone pair electron delocalization and negative inductive effects, suggesting the location of Li at a distance from the amide short enough to produce variations in the force constants associated with these vibrations. Similarly, the change in the pyridyl out-of-plane ring deformation vibrations ($\Delta\omega$ = −7.5 cm^{-1}) could result from the altered destabilization of the *pia* aromatic π electrons, due to the influence of the electrophilic character of lithium near the amide and the pyridyl free nitrogen site. Effects over the amide I bands related to the displacement of the CO stretching vibrations ($\Delta\omega$ = −4.9 cm^{-1}), caused by emerging forces of interaction over the amide oxygen by an electrophile, could influence the carbonyl covalency and force constants. The pyridyl CC and CN stretching vibrations also showed a frequency shift to lower values ($\Delta\omega$ = −4 cm^{-1}), probably induced by mesomeric effects due to the filling of the free donor site at the pyridyl nitrogen lone pair occurring simultaneously with the already mentioned *pia* aromatic π-electron-cloud destabilization and the amide group modification. This shift could also involve changes of the amide II bands, in which the uneven bending deformation is restricted and weakened due to electronic variations at the amide nitrogen produced by the proximity of lithium and the amide induction effect, an observation congruent with the noted decrease in relative intensity (at ∼1613.9 cm^{-1} in Figure 5).

On the other hand, changes in the copper in-plane bending vibrations at equatorial positions ($\Delta\omega$ = +2.7 cm^{-1}) could be due to a strengthening interaction, which is also manifested in the changes probably related to stretching vibrations of CuO and CuN at equatorial positions ($\Delta\omega$ = −5.1 cm^{-1}) as bonding shortens. Curiously, bands related to the CuN bending tilt deformation at axial positions followed an opposite trend ($\Delta\omega$ = −1.3 cm^{-1}), denoting the possible existence of an attenuated distortion typically found due to the Jahn−Teller effect. This distortion can be inferred from crystallographic results obtained around the coordination of copper after lithiation as well. Other less representative but equally relevant changes include the amide NH out-of-plane deformation bands ($\Delta\omega$ = +2.4 cm^{-1}), in which enlarged nonbonding interactions could have produced this increased frequency of vibration, and the pyrazine ring deformation bands ($\Delta\omega$ = −2.4 cm^{-1}) that indicate a stabilization of this heterocycle. Additionally, a group of band frequencies remained at the same position after lithiation, such as some of the equatorial bending and symmetric bridge stretching vibrations around copper, i.e., 230.9 and 360.5 cm^{-1}, in agreement with the possible attenuated octahedral distortion previously mentioned. Furthermore, the invariability of other contributions to the NH out-of-plane deformation bands (784.6 cm^{-1}) happening in addition to these changes could manifest local disorder effects of noncovalent interactions.

Unvarying bands suggesting that the *pzdc* ligand remained unmodified include the pyrazine CCC bending (658.5 cm^{-1}), pyrazine CCCN, CCOO, CH, and N-ring out-of-plane

https://dx.doi.org/10.1021/acs.cgd.0c00202
Cryst. Growth Des. 2020, 20, 3898−3912

bending and CO in-plane bending (784.6 cm^{-1}), and the ring in-plane deformation vibrations (1063.2 cm^{-1}). Other typical bands such as the pyrazine CH in-plane bending and CC and CN stretching vibration contributions also displayed small blue and red shifts ($\Delta\omega \leq \pm 1$ cm^{-1}). However, the change observed for pyrazine CC and CN stretching and ring breathing vibrations ($\Delta\omega = -3.3$ cm^{-1}) could result from a displacement in the electron distribution of the aromatic ring due to structural partial distortion effects. The COO groups of *pzdc* showed in-plane and out-of-plane bending vibration changes ($\Delta\omega \leq +1$ cm^{-1}), which in addition to the reduced gap in the difference between COO symmetric and asymmetric stretching bands after the modification hinted to no significant variations in electron distribution.

Regardless of the complex crystal lattice and nonbonding interactions of the PCPs under study here, the group frequency approximation interpreted from Raman shifts offered chemical evidence of the framework lithiation (Table 2). Similarly, Raman measurements for $Cu_2(pzdc)_2(dpyg)$ before and after lithiation showed other apparent variations related to the functionalization approach for future analysis (Figure S-5b in the Supporting Information). Complementary evidence of lithium to framework bonding was inspected by the resemblance of the spectra from Figure 5 to the alkoxide assignments available in the literature (i.e., NaO stretching bands for the NaO-*tert*-butoxide spectrum). The stretching vibrations expected for the LiO counterpart probably contributed to new features peaking at 212.7 cm^{-1}, while the corresponding peaks for CO and CC stretching and OC-$(CH_3)_3$ and CH_3 bending from skeletal bands that would originate from an eventual *tert*-alkoxide or *tert*-butane group were absent.

Other bands of interest that emerged after the modification show contributions to LiN bending vibrations at the *pia* nitrogen lone pair of the pyridyl ring, which could explain the observed increase in intensity at ~164 cm^{-1}. The hypothesis of pyridyl nitrogen site occupation by lithium is coherent with new bands that appeared after the modification at 446.2 and 644 cm^{-1}, probably corresponding to LiN stretching vibrations. Additional evidence of disturbance in this *pia* nitrogen lone pair electron ambience includes not only the slight blue shifts of the pyridyl ring breathing vibrations at 847.8 and 1027.4 cm^{-1} ($\Delta\omega \approx +1$ cm^{-1}) but also slight red shifts on the out-of-plane pyridyl ring deformation vibrations at 706.4 and 752.8 cm^{-1}. These blue shifts are typically observed on bonding formation at the nitrogen position in pyridine-like rings; while the red shifts could indicate the presence of two *pia* pyridyl rings energetically surrounded in a different way or slight changes in π-stacking interactions. Therefore, the available donor sites of Cu(*pzdc*)(*pia*), such as the amide nitrogen, the carbonyl oxygen, and the pyridyl ring free nitrogen from *pia* ligands, are more likely to constitute positions for lithium, in contrast to the pyrazine ring nitrogen and the carbonyl oxygen from *pzdc* ligand on the basis of scarcer evidence of frequency variations found for these bands.

3.3. CO_2 Adsorption Enhancement. Figure 6 presents the CO_2 equilibrium adsorption and desorption isotherm gathered up to 7 bar at 298 K for the lithiated PCP Cu(*pzdc*)(*pia*)$(LiO)_3$. The adsorbed amount increased as a function of pressure without reaching a saturation plateau within the prescribed gas pressure range. The increase in loading turned more notorious with CO_2 pressure increments approaching 7 atm, depicting a concave up adsorption path.

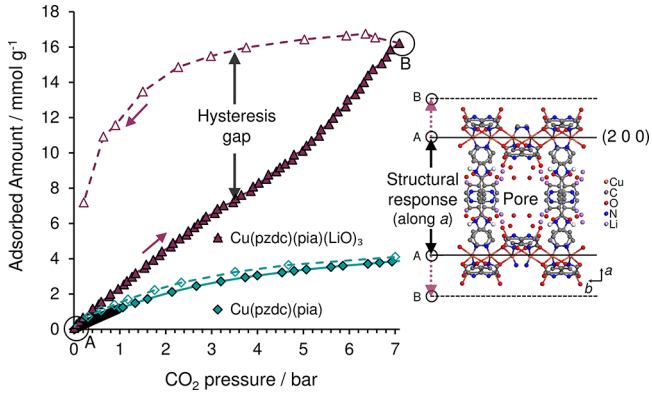

Figure 6. (left) CO_2 equilibrium adsorption (filled symbols) and desorption (open symbols) isotherms for Cu(*pzdc*)(*pia*) and Cu(*pzdc*)(*pia*)$(LiO)_3$ at 298 K. (right) Schematics of the PCP structural response concomitant with the CO_2 adsorption from point A to B, for the indexed (200) crystallographic planes along the *a* axis.

The adsorption behavior of the lithiated PCP is significantly different from CO_2 adsorption results previously reported at the same temperature for Cu(*pzdc*)(*pia*) by Hernandez-Maldonado and co-workers.[14] Cu(*pzdc*)(*pia*) showed a concave down isotherm and did not exhibit a definitive loading plateau within a 0−8 bar pressure range. The maximum CO_2 adsorption loading observed for Cu(*pzdc*)(*pia*) at 7 bar was 3.2 mmol g^{-1}.[14] At the same gas pressure, the lithiated PCP has a loading that is a factor of 5 larger than that of Cu(*pzdc*)(*pia*), providing clear evidence of stronger adsorbate−adsorbent interactions due to the presence of lithium.

Figure 6 shows pronounced hysteresis in desorption, which is also evidence for stronger adsorbate−adsorbent interactions as a result of the lithiation. Hysteretic adsorption−desorption has been reported by Hernandez-Maldonado and co-workers for other isoreticular PCPs during CO_2 adsorption measurements up to 8 atm at ambient temperature.[14,15] However, the lithiated framework in this work depicted an unusual and pronounced adsorption path evolution. Cu(*pzdc*)(*pia*) is microporous with a surface area of ca. 400 m^2 g^{-1} and a micropore volume of ca. 0.1 cm^3 g^{-1}.[14] Calculations of Conolly pore volume obtained for the unit cell model excluding any solvent before and after lithiation are 0.16 and 0.05 cm^3 g^{-1}, respectively. These values translate to CO_2 maximum loadings of ca. 2.5 and 0.8 mmol g^{-1} in the PCP before and after lithiation, respectively, assuming that the CO_2 is packed within the pores with a density similar to that of a liquid state. The larger loadings observed at high pressure (Figure 6) are therefore an indication of pressure-induced structural flexibility.

The increase in the CO_2 adsorption amount is likely due not only to the inclusion of lithium but also to the formation of adsorption sites in positions exposed to the pore channels, where CO_2 can interact without much steric hindrance. Computational studies suggest that CO_2 is attracted to Cu nodes of PCPs but that such an interaction is limited due to shielding of the nodes by adjacent ligand functional groups.[15] In terms of gas−adsorbent interaction forces, the incorporation of lithium could influence the adsorption site polarizability, which is known to play a key role in the contributions to the potential of adsorption. The polarizability would be 3 orders of magnitude larger for a covalently incorporated lithium atom

https://dx.doi.org/10.1021/acs.cgd.0c00202
Cryst. Growth Des. 2020, 20, 3898−3912

versus one weakly physisorbed as a cation (i.e., weakly attracted to heterocycle electron-rich clouds or similar). Also, polarizability values can be 1 order of magnitude larger in comparison to other atoms already present in the backbone of the PCP framework such as carbon, nitrogen, and oxygen. Thus, the observed 2- and up to 4-fold adsorption uptake improvements seen in Cu(*pzdc*)(*pia*)$(LiO)_3$ (i.e., Figure 6), if derived solely from nonelectrostatic interaction potentials, could agree with the conformation of adsorption sites with Li-bond to porous surface approaching covalency, considering that these potentials, such as the combined dispersion and repulsion energies, typically involve terms with polarizability in an almost direct proportion to the adsorption uptake.

Similarly, the small atomic radii of lithium could advantageously introduce internuclear distances with lower values for the adsorption interacting pairs at the new sites. This is beneficial, since the interacting pair distance is inversely proportional to the nonspecific and specific interaction potentials, the latter including the interaction of a CO_2 permanent quadrupole with the electric field gradient of the surface.[19] Further, the conformation of new lithium-based sites over the *pia* ligands probably induces overlapping of the surface potential in areas nonhindered to the adsorbate, favoring mass transport conditions even when the pressure is increased. The premise is perhaps in agreement with the CO_2 tendency to follow zones with high electrostatic potentials along the pores during the adsorption, but whether this mechanism is explicitly occurring in Cu(*pzdc*)(*pia*)$(LiO)_3$ will require further investigation. An increase in the Li content could also produce a larger CO_2 uptake if new adsorption sites decorate the pore surface. Exploration of the limit of Li incorporation may require additional functionalization steps to avoid structural decomposition, as the high basicity of the Li precursor could decompose the framework.

The pronounced hysteresis shown in Figure 6 also suggests a distinctive adsorption mechanism closely related to induced structural distortions. Indeed, the gap between the leg of adsorption and desorption (i.e., hysteresis gap) at an intermediate pressure of 3.5 bar was ca. 28 times superior to the value estimated from measurements reported previously by our group for Cu(*pzdc*)(*pia*).[15] During adsorption, the physicochemical properties of the adsorbed phase could differ from those found in the bulk phase (i.e., liquid, solid, or gaseous) at a fixed thermodynamic state. A similar behavior may be found for a porous flexible framework in comparison to rigid structures. If both factors operate simultaneously, the fluctuations on the crystal free energy change due to induced structural transitions could be typically connected to hysteretic or stepped adsorption isotherms, which could still lead to gas uptake mechanisms divergent from the micropore filling or the capillary condensation seen for some stiff structures that are yet under research currently. Therefore, the hysteretic desorption stage observed in Figure 6 probably involves a 3-fold interrelated effect originating from (1) an increase in the potential of interactions anchoring the CO_2 to the framework, (2) an adsorbed phase electron density located at positions unresponsive to mild negative changes in gas pressure, possibly obeying a reinforced interaction by the whole structure stability through cooperative effects from the aromatic ring $\pi-\pi$ stacking, combined with the influence of contiguous pores sharing boundary wall-ligands in three dimensions, and (3) an increase in the minimum energy of the structural rearrangement required for the progression and achievement of the desorption. Room-temperature CO_2 adsorption results (Figure S-6 in the Supporting Information) of lithiated $Cu_2(pzdc)_2(dpyg)$ (i.e., isoreticular pillared-layer network holding *dpyg* pillars with hydroxy groups) showed a moderate improvement in the adsorbed amount in comparison to adsorption values obtained before the modification[15] (i.e., maximum improvement in loading up to 2.7-fold), added to a hysteresis gap at 3.5 bar without apparent change, indicating that the attained pore surface modification was less effective toward the improvement of the adsorption of CO_2.

An attempt to quantify the level of interactions between CO_2 and either of the lithiated Cu(*pzdc*)(*pia*) or $Cu_2(pzdc)_2(dpyg)$ PCPs was made via the desorption legs of the data shown in Figures 6, Figure S-6, and eq 1. The resulting Dubinin–Astakhov isotherm model parameters and heat of desorption profiles are shown in Table 3 and Figure 7,

Table 3. Dubinin–Astakhov (DA) Isotherm Model Parameters from CO_2 Desorption Isotherms at 25 °C

	DA isotherm params			
adsorbent	q_o (mmol/g)	$\beta_{DA}E$ (kJ/mol)	n	std dev
Cu(*pzdc*)(*pia*)$(LiO)_3$	17.705	14.536	2.964	±0.145
lithiated $Cu_2(pzdc)_2(dpyg)$	1.516	17.083	7.133	±0.059

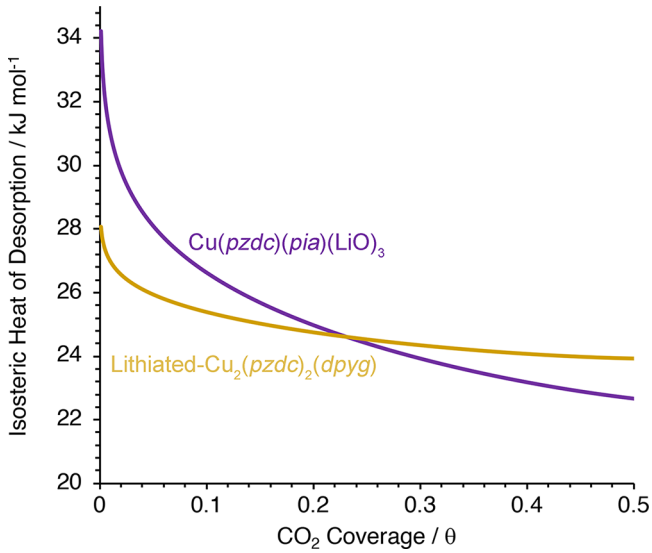

Figure 7. CO_2 heat of desorption profiles. Adsorbate coverage is defined as $\theta = q/q_0$.

respectively. The steep slope of the heat profile for Cu(*pzdc*)-(*pia*)$(LiO)_3$ at near-zero coverage evidences CO_2 interactions with the material that are much stronger in comparison to those in the lithiated $Cu_2(pzdc)_2(dpyg)$. Interestingly, the desorption energy parameter ($\beta_{DA}E$) as estimated from a fit of the Dubinin–Astakhov isotherm model (eq 2 and Table 3) is similar in both PCPs, but the heterogeneity parameters (n) are quite different. This could be plausibly interpreted as dominance of the lithium-containing sites in terms of adsorption sites and surface homogeneity.

The near-zero CO_2 loading heats of these lithiated PCPs are also larger than those of the nonlithiated Cu(*pzdc*)(*pia*) or $Cu_2(pzdc)_2(dpyg)$ reported previously by Hernandez-Maldonado and co-workers.[14] For example, the near-zero CO_2 loading heat of adsorption observed in nonlithiated Cu(*pzdc*)-

https://dx.doi.org/10.1021/acs.cgd.0c00202
Cryst. Growth Des. 2020, 20, 3898–3912

(*pia*) is ca. 27 kJ mol^{-1},[14] in comparison to ca. 34 kJ mol^{-1} in the lithiated counterpart. In the case of Cu$_2$(*pzdc*)$_2$(*dpyg*), the heats at near-zero CO_2 loadings are ca. 12 and 28 kJ mol^{-1} for the nonlithiated[14] and lithiated PCP, respectively, which evidence considerable interactions between the lithium-containing surface and the adsorbate.

3.4. Structural Framework Distortion upon CO_2 Adsorption. *In situ* adsorption and powder X-ray diffraction experiments conducted under CO_2 and N_2 pressures as high as 50 and 15 bar, respectively, at ambient temperature allowed a direct observation of the structural changes suggested by the adsorption results discussed above. The sequence of diffraction patterns presented in Figure 8 was measured following a cycle

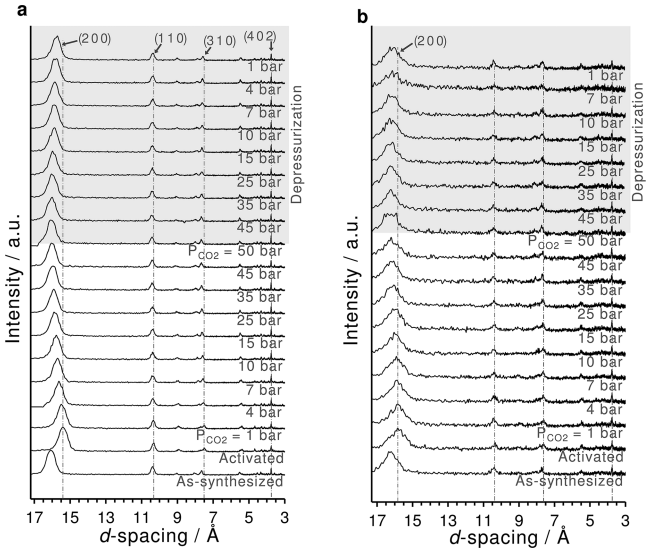

Figure 8. *In situ* powder X-ray diffraction and CO_2 adsorption for (a) Cu(*pzdc*)(*pia*) and (b) Cu(*pzdc*)(*pia*)(LiO)$_3$. The patterns labeled "As-synthesized" correspond to the as-synthesized material containing sorbed synthesis solvent, and the "Activated" label corresponds to materials scanned immediately after the activation stage (i.e., powder kept under a N_2 gas atmosphere; P_{CO_2} = 0 bar, P_{N_2} = 1 bar).

of CO_2 pressurization−depressurization for Cu(*pzdc*)(*pia*) and Cu(*pzdc*)(*pia*)(LiO)$_3$. The pattern recorded immediately after the activation of the samples (labeled "Activated" in Figure 8) was interpreted as a guest-free structure, in which several peak positions were displaced without the dismantlement of the frameworks and ,therefore, were used to portray a criterion an the analysis of the forthcoming structural changes along the cycle. The diffraction peak shifting gradually progressed with the CO_2 pressure increase, depicting changes toward a pattern apparently like that recorded before the activation stage ("As-synthesized" in Figure 8). Once the CO_2 pressure was reduced, the peak positions shifted toward the positions of the pattern acquired immediately after activation. The path of the angular shifts is not consistent with a phase change and instead provides structural evidence of CO_2 loading in the pores of the framework. The most intense reflection for both PCPs, indexed as the (200) crystallographic plane, showed a *d* spacing shift to higher values until the maximum pressure of 50 bar was attained. The reduction in CO_2 pressure produced a shift of this reflection to lower *d* spacing, a behavior correlated with a pressure-induced expansion−contraction structural response. Comparatively, the same reflection for a cycle under nitrogen also showed variations, as a result of negligible adsorption or just pressure effects (Figure S-7 in the Supporting Information).

The structural variations of Cu(*pzdc*)(*pia*) and Cu(*pzdc*)(*pia*)(LiO)$_3$ during the CO_2 adsorption−desorption cycle were analyzed geometrically by assigning the Cu positions to nodes that subsequently dictated the orientation of the organic building blocks. The layers were pictured as a set of flat two-dimensional meshes parallel to the crystallographic *bc* plane. A projection of the lattice into the plane *ab* or *ac* displays the ordered parallel layering and the alignment of the nearby pillars, in which the pyridyl rings are placed one in front of another, generating the porous channels along the *c* axis, as illustrated in Figure 3.

Figure 9 shows the changes in *d* spacing, Δd, as a function of CO_2 and N_2 pressure for (200) and other key indexed reflections of Cu(*pzdc*)(*pia*) before and after lithiation. The set of changes for CO_2 experiments revealed structural distortion variations with different magnitudes in each crystallographic direction. The changes in *d* spacing for the high-intensity indexed reflections (200), (110), (310), and (402) were used to understand the structural changes with pressure through the crystallographic *ab* and *ac* planes, which are related to the porous cavities (i.e., along the *c* axis). The larger changes in *d* spacing corresponded to the (200) planes (Figure 6 (right) and Figure 9), which evidenced the variations along the *a* axis as an essential determining factor in the structural response, specifically for the adsorption of CO_2. The observed changes in the (200) planes for Cu(*pzdc*)(*pia*) in N_2 experiments (Figure 9b) shed light on the flexibility of this structure even in response to low quadrupole moment molecules such as N_2, for the pressure range covered. The structural changes that were observed for the as-prepared and lithiated samples under N_2 take place under weak adsorption interaction forces. Figure 9b,d shows that the full structural reversibility was not reached by the end of the pressurization and depressurization cycles. Thus, the complete isothermal structural recovery may require an additional step (i.e, vacuum).

Figure 10 shows *d* spacing and Δd for the (200) reflection for frameworks with *pia* and *dpyg* pillar ligands (i.e., Cu(*pzdc*)(*pia*) and Cu$_2$(*pzdc*)$_2$(*dpyg*), in which *dpyg* pillars contain hydroxy groups). At CO_2 pressures below 10 bar, the *d* spacing for Cu(*pzdc*)(*pia*)(LiO)$_3$ displayed a different behavior in comparison to the nonmodified material (Figure 10a). A concave up shape in *d* spacing and Δd for the same pressure range indicates that the enhancement in the CO_2 adsorbed amount after lithiation (Figure 6) and the induced structural enlargement along the *a* axis may be directly related.

The key result from the structural variations implied in Figure 10 is that the lithiation appears to yield Li sites directed toward *pia* ligands on the internal pore surface. Several observations support this conclusion. First, the alternative case, in which Li is instead absorbed on the external surface of the large PCP crystallites, would not yield distinct structural behavior along the crystallographic axes of the crystal during CO_2 adsorption. Further, before any CO_2−adsorbent interaction (P_{CO_2} = 0 bar), this lithiated framework showed a *d* spacing 2.6% larger than that for the nonmodified PCP (Figure 10a), indicating a pore enlargement along the *a* axis, which agrees with the slight increase in the *a* lattice parameter. Even though the refinement results also reveal a diminishment in the unit cell volume (∼1.6%), it could be attributed to structural distortions as a result of the increase in the crystallographic β

https://dx.doi.org/10.1021/acs.cgd.0c00202
Cryst. Growth Des. 2020, 20, 3898−3912

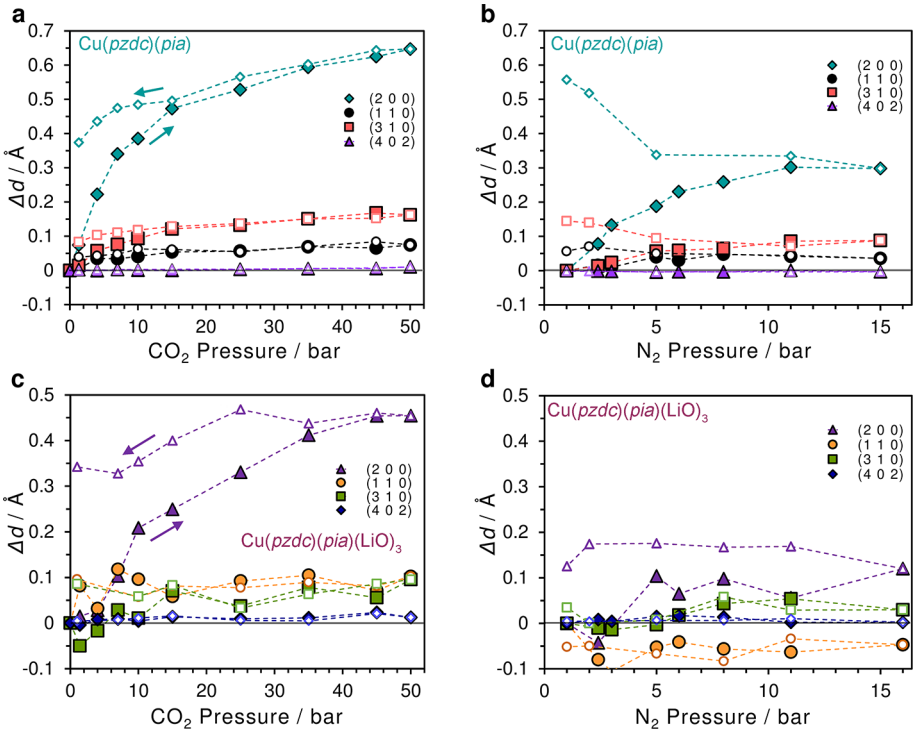

Figure 9. Change in spacing ($\Delta d = d - d_{activated}$) for the indexed crystallographic planes (200), (110), (310), and (402), estimated from *in situ* powder X-ray diffraction measurements over a cycle of gas-driven pressurization (filled symbols) and depressurization (open symbols) corresponding to the adsorption and desorption of CO_2 and N_2. (a) and (b) are for Cu(*pzdc*)(*pia*). (c) and (d) are for Cu(*pzdc*)(*pia*)$(LiO)_3$. $d_{activated}$ corresponds to the *d* spacing estimated for each material right after the activation stage (i.e., powder kept under a N_2 atmosphere, also referring to $P_{CO_2} = 0$ bar and $P_{N_2} = 1$ bar). The dotted lines were added connecting consecutive points only for better overall visualization of each cycle path.

lattice parameter. Finally, and most importantly, Δd during the pressurization stage is larger for both PCPs before lithiation (Figure 10c,d), indicating that the adsorption was happening under nonequivalent porous environments. Variations in adsorption energy, pore size, and shape could explain the improvements in the adsorbed amount previously discussed, consequent to the enriched surface energetics obtained after lithiation.

The *d* spacing and Δd for $Cu_2(pzdc)_2(dpyg)$, i.e., PCP with pillars with hydroxy groups, also exhibited a change in behavior with functionalization when the CO_2 pressure was increased (Figure 10b,d), although moderate CO_2 adsorption enhancements were achieved for the same material after lithiation (Figure S-8). Measurements under N_2 for this material showed no significant changes before and after lithiation (Figure 10f). It is important to note that, although the heat of desorption profiles (Figure 7) suggest that the lithiation of Cu(*pzdc*)(*pia*) and $Cu_2(pzdc)_2(dpyg)$ was capable of improving the near-zero CO_2 loading in both cases, the *in situ* diffraction experiments under N_2, which has a much smaller quadrupole moment in comparison to CO_2, hence correspond to measurements of structural responses under considerably low adsorption interaction forces. Therefore, the structural changes shown in Figure 10e for Cu(*pzdc*)(*pia*)$(LiO)_3$ are mainly associated with cooperative stress, physical strain, and other structural factors, such as the micropore volume and shape. A synergy, which can play a key role in adsorption, between the structural response and the isosteric heat improvement produced after lithiation was not observed under N_2 for lithiated-$Cu_2(pzdc)_2(dpyg)$ (Figure 10f). Thus, the lithiation effects on the structural response along with the adsorption uptake improvements demonstrate a lower performance for the PCP with pillars with a hydroxy versus an amide functionality.

4. CONCLUSIONS

This work reveals a connection between amide functional groups located along the pore channels of a pillared layer porous coordination polymer, Cu(*pzdc*)(*pia*), and the effects of lithiation on CO_2 adsorption at room temperature. Similar results may be possible with other alkali-metal alkoxide functionalization steps. The incorporation of Li into this PCP results in dramatic increases in CO_2 adsorption, which can be linked directly to enhancements in the pore surface electric field potential of interaction. Synchrotron powder X-ray diffraction and Rietveld refinement revealed a porous crystal structure with a pore size accommodating rapid CO_2 transport. This crystal structure is observed both before and after lithiation. Elemental and thermal gravimetric analyses, with results from the fitted structural model, showed a Li incorporation of 3 Li atoms per asymmetric unit. Further, Raman spectroscopy showed that LiO units were found proximal to the lone pair of the *pia* amide and pyridyl groups. The CO_2 adsorption isotherm gathered at 25 °C and up to 7 bar for Cu(*pzdc*)(*pia*)$(LiO)_3$ showed gas uptake enhancements of at least 1 order of magnitude greater than those of the material before lithiation. Furthermore, a concave up behavior with notorious hysteresis indicated the internal pore surface modification, in which structural flexibility effects take place due to the presence of new or stronger adsorption sites influencing the adsorbed phase. CO_2 adsorption and *in situ* X-

https://dx.doi.org/10.1021/acs.cgd.0c00202
Cryst. Growth Des. 2020, 20, 3898−3912

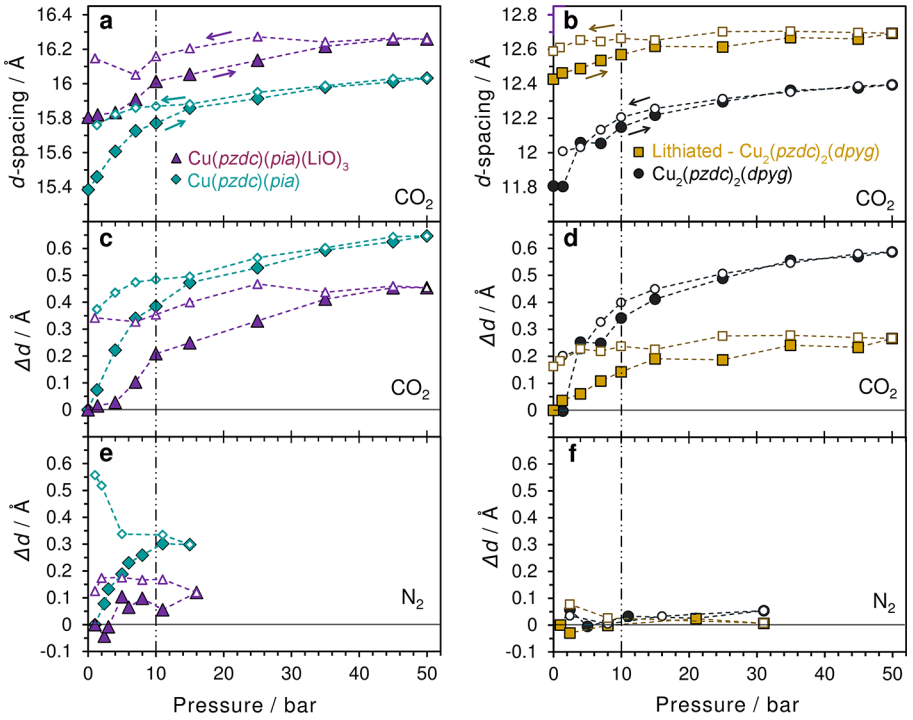

Figure 10. (a, b) Evolution of *d* spacing and (c–f) change in *d* spacing ($\Delta d = d - d_{activated}$) for the most intense reflection from *in situ* powder X-ray diffraction measurements for a cycle of a gas-driven pressurization (filled symbols) and depressurization (open symbols) corresponding to the adsorption and desorption of CO_2 and N_2 for Cu(*pzdc*)(*pia*) and Cu(*pzdc*)(*pia*)$(LiO)_3$, shown in (a), (c), and (e), and Cu_2(*pzdc*)$_2$(*dpyg*) and ,odified-Cu_2(*pzdc*)$_2$(*dpyg*), shown in (b), (d), and (f). $d_{activated}$ corresponds to the *d* spacing of each material immediately after the activation stage, when the solid is kept solely under a N_2 atmosphere, also referring to P_{CO_2} = 0 bar and a P_{N_2} = 1 bar. The dotted lines were added connecting consecutive points only for better overall visualization of each cycle path.

ray powder diffraction experiments at up to 50 bar at ambient temperature were used for the observation of the structural response alongside this process. Changes in 2θ angles with pressure for the most intense reflection in successive powder X-ray diffraction patterns were interpreted through *d* spacing variations in the crystallographic (200) planes. During the pressurization stage, at pressures below 10 bar, the *d* spacing pathway resembled the behavior followed by the CO_2 adsorption uptake for a similar pressure range, indicating possible new cooperative structural global distortions induced by CO_2 pressure and triggered by effects of narrow and strong surface potential alterations produced by the functionalization.

■ ASSOCIATED CONTENT

Supporting Information

The Supporting Information is available free of charge at https://pubs.acs.org/doi/10.1021/acs.cgd.0c00202.

Figures S1–S8, as described in the text (PDF)

Accession Codes

CCDC 1952587–1952588 contain the supplementary crystallographic data for this paper. These data can be obtained free of charge via www.ccdc.cam.ac.uk/data_request/cif, or by emailing data_request@ccdc.cam.ac.uk, or by contacting The Cambridge Crystallographic Data Centre, 12 Union Road, Cambridge CB2 1EZ, UK; fax: +44 1223 336033.

■ AUTHOR INFORMATION

Corresponding Author

Arturo J. Hernández-Maldonado − *Department of Chemical Engineering, University of Puerto Rico-Mayagüez Campus, Mayagüez, Puerto Rico 00681-9000, United States;* orcid.org/0000-0001-9379-8987; Phone: 787-832-4040; Email: arturoj.hernandez@upr.edu; Fax: 787-834-3655

Authors

Karina Riascos-Rodríguez − *Department of Chemical Engineering, University of Puerto Rico-Mayagüez Campus, Mayagüez, Puerto Rico 00681-9000, United States*

Samuel Marks − *Department of Materials Science and Engineering, University of Wisconsin-Madison, Madison, Wisconsin 53706, United States*

Paul G. Evans − *Department of Materials Science and Engineering, University of Wisconsin-Madison, Madison, Wisconsin 53706, United States;* orcid.org/0000-0003-0421-6792

Samuel P. Hernández-Rivera − *Department of Chemistry, University of Puerto Rico-Mayagüez Campus, Mayagüez, Puerto Rico 00681-9000, United States*

Jose L. Ruiz-Caballero − *Department of Chemistry, University of Puerto Rico-Mayagüez Campus, Mayagüez, Puerto Rico 00681-9000, United States*

Dalice Piñero − *Department of Chemistry, University of Puerto Rico-Rio Piedras Campus, San Juan, Puerto Rico 00931-3346, United States*

Complete contact information is available at: https://pubs.acs.org/10.1021/acs.cgd.0c00202

Notes

The authors declare no competing financial interest.

https://dx.doi.org/10.1021/acs.cgd.0c00202
Cryst. Growth Des. 2020, 20, 3898–3912

■ ACKNOWLEDGMENTS

The authors thankfully acknowledge the support of this research from the Puerto Rico Institute for Functional Materials Graduate Fellowship Program under the NSF Award No. EPS-1002410 and partial support of this research by the NSF through the University of Wisconsin Materials Research Science and Engineering Center under Award No. DMR-1720415. Funding for this work was provided by the National Science Foundation (NSF) Partnership for Research and Education in Materials (PREM) Awards DMR-0934115 and DMR-1827894.

■ REFERENCES

(1) Olivier, J. G. J.; Schure, K. M.; Peters, J. A. H. W. *Trends in Global CO2 and Total Greenhouse Gas Emissions*; PBL Netherlands Environmental Assessment Agency: 2017.

(2) UNEP *The Emissions Gap Report 2018*; 9789280737264; United Nations Environment Programme: Nairobi, 2018.

(3) Bui, M.; Adjiman, C. S.; Bardow, A.; Anthony, E. J.; Boston, A.; Brown, S.; Fennell, P. S.; Fuss, S.; Galindo, A.; Hackett, L. A.; Hallett, J. P.; Herzog, H. J.; Jackson, G.; Kemper, J.; Krevor, S.; Maitland, G. C.; Matuszewski, M.; Metcalfe, I. S.; Petit, C.; Puxty, G.; Reimer, J.; Reiner, D. M.; Rubin, E. S.; Scott, S. A.; Shah, N.; Smit, B.; Trusler, J. P. M.; Webley, P.; Wilcox, J.; Mac Dowell, N. Carbon Capture and Storage (CCS): The Way Forward. *Energy Environ. Sci.* **2018**, *11*, 1062−1176.

(4) Li, H.; Wang, K.; Sun, Y.; Lollar, C. T.; Li, J.; Zhou, H.-c. Recent Advances in Gas Storage and Separation Using Metal−Organic Frameworks. *Mater. Today* **2018**, *21*, 108−121.

(5) Cohen, S. M. Postsynthetic Methods for the Functionalization of Metal-Organic Frameworks. *Chem. Rev.* **2012**, *112*, 970−1000.

(6) Kumar, P.; Kim, K. H.; Kwon, E. E.; Szulejko, J. E. Metal-Organic Frameworks for the Control and Management of Air Quality: Advances and Future Direction. *J. Mater. Chem. A* **2016**, *4*, 345−361.

(7) Kitaura, R.; Kitagawa, S.; Kubota, Y.; Kobayashi, T. C.; Kindo, K.; Mita, Y.; Matsuo, A.; Kobayashi, M.; Chang, H.-C.; Ozawa, T. C.; Suzuki, M.; Sakata, M.; Takata, M. Formation of a One-Dimensional Array of Oxygen in a Microporous Metal-Organic Solid. *Science* **2002**, *298*, 2358−2361.

(8) Kitaura, R.; Fujimoto, K.; Noro, S.-i.; Kondo, M.; Kitagawa, S. A Pillared-Layer Coordination Polymer Network Displaying Hysteretic Sorption: $[Cu_2(pzdc)_2(dpyg)]n$ (pzdc = Pyrazine-2,3-dicarboxylate; dpyg = 1,2-Di(4-pyridyl)-glycol). *Angew. Chem., Int. Ed.* **2002**, *41*, 133−135.

(9) Matsuda, R.; Kitaura, R.; Kitagawa, S.; Kubota, Y.; Kobayashi, T. C.; Horike, S.; Takata, M. Guest Shape-Responsive Fitting of Porous Coordination Polymer with Shrinkable Framework. *J. Am. Chem. Soc.* **2004**, *126*, 14063−14070.

(10) Uemura, K.; Matsuda, R.; Kitagawa, S. Flexible Microporous Coordination Polymers. *J. Solid State Chem.* **2005**, *178*, 2420−2429.

(11) Kitagawa, S.; Matsuda, R. Chemistry of Coordination Space of Porous Coordination Polymers. *Coord. Chem. Rev.* **2007**, *251*, 2490−2509.

(12) Sakamoto, H.; Kitaura, R.; Matsuda, R.; Kitagawa, S.; Kubota, Y.; Takata, M. Systematic Construction of Porous Coordination Pillared-layer Structures and Their Sorption Properties. *Chem. Lett.* **2010**, *39*, 218−219.

(13) García-Ricard, O. J.; Hernández-Maldonado, A. J. Cu_2(pyrazine-2,3-dicarboxylate)$_2$(4,4′-bipyridine) Porous Coordination Sorbents: ActivationTemperature, Textural Properties, and CO_2 Adsorption at Low Pressure Range. *J. Phys. Chem. C* **2010**, *114*, 1827−1834.

(14) García-Ricard, O. J.; Silva-Martínez, J. C.; Hernández-Maldonado, A. J. Systematic Evaluation of Textural Properties, Activation Temperature and Gas Uptake of $Cu_2(pzdc)_2L$ [L = Dipyridyl-Based Ligands] Porous Coordination Pillared-Layer Networks. *Dalton Trans.* **2012**, *41*, 8922−8930.

(15) García-Ricard, O. J.; Meza-Morales, P.; Silva-Martínez, J. C.; Curet-Arana, M. C.; Hogan, J. A.; Hernández-Maldonado, A. J. Carbon Dioxide Storage and Sustained Delivery by $Cu_2(pzdc)_2L$ [L = Dipyridyl-Based Ligand] Pillared-Layer Porous Coordination Networks. *Microporous Mesoporous Mater.* **2013**, *177*, 54−58.

(16) Riascos-Rodríguez, K.; Schroeder, A. J.; Arend, M. R.; Evans, P. G.; Hernández-Maldonado, A. J. Hysteretic Adsorption of CO_2 onto a Cu_2(pzdc$_2$(bpy) Porous Coordination Polymer and Concomitant Framework Distortion. *Dalton Trans.* **2014**, *43*, 10877−10884.

(17) Hernández-Maldonado, A. J.; Arrieta-Pérez, R. R.; Primera-Pedrozo, J. N.; Exley, J. Structure of a Porous $Cu_2(pzdc)_2$(bpp) (pzdc: Pyrazine-2,3-dicarboxylate, bpp: 1,3-Bis(4-pyridyl)propane) Coordination Polymer and Flexibility upon Concomitant Hysteretic CO_2Adsorption. *Cryst. Growth Des.* **2015**, *15*, 4123−4131.

(18) Chen, H.; Riascos-Rodríguez, K.; Marcano-González, M. E.; Hernández-Maldonado, A. J. $Cu_2(pzdc)_2L$ [L = Dipyridyl-Based Ligands] Porous Coordination Polymers: Hysteretic Adsorption and Diffusion Kinetics of CO_2 and CH_4. *Chem. Eng. J.* **2016**, *283*, 806−815.

(19) Yang, R. T. *Adsorbents: Fundamentals and Applications*; Wiley: Hoboken, NJ, 2003.

(20) Gu, C.; Liu, Y.; Liu, J.; Hu, J.; Wang, W. Ab Initio Study of Gas Adsorption in Metal-Organic Frameworks Modified by Lithium: The Significant Role of Li-Containing Functional Groups. *J. Phys. Chem. C* **2018**, *122*, 18395−18404.

(21) Evans, J. D.; Sumby, C. J.; Doonan, C. J. Post-Synthetic Metalation of Metal-Organic Frameworks. *Chem. Soc. Rev.* **2014**, *43*, 5933−5951.

(22) Kanoo, P.; Matsuda, R.; Sato, H.; Li, L.; Jeon, H. J.; Kitagawa, S. In Situ Generation of Functionality in a Reactive Haloalkane-Based Ligand for the Design of New Porous Coordination Polymers. *Inorg. Chem.* **2013**, *52*, 10735−10737.

(23) Long, J. R.; Bloch, E. D.; Britt, D.; Lee, C.; Doonan, C. J.; Uribe-Romo, F. J.; Furukawa, H.; Yaghi, O. M. Metal Insertion in a Microporous Metal-Organic Framework Lined with 2,2 ’-Bipyridine. *J. Am. Chem. Soc.* **2010**, *132*, 14382−14384.

(24) Wei, Z.; Yuan, D.; Zhao, X.; Sun, D.; Zhou, H. C. Linker Extension Through Hard-Soft Selective Metal Coordination for the Construction of a Non-Rigid Metal-Organic Framework. *Sci. China: Chem.* **2013**, *56*, 418−422.

(25) Nugent, P.; Belmabkhout, Y.; Burd, S. D.; Cairns, A. J.; Luebke, R.; Forrest, K.; Pham, T.; Ma, S.; Space, B.; LukaszWojtas; Eddaoudi, M.; Zaworotko, M. J. Porous Materials with Optimal Adsorption Thermodynamics and Kinetics For CO_2 Separation. *Nature* **2013**, *495*, 80−84.

(26) Bhatt, P. M.; Belmabkhout, Y.; Cadiau, A.; Adil, K.; Shekhah, O.; Shkurenko, A.; Barbour, L. J.; Eddaoudi, M. A Fine-Tuned Fluorinated MOF Addresses the Needs for Trace CO_2 Removal and Air Capture Using Physisorption. *J. Am. Chem. Soc.* **2016**, *138*, 9301−9307.

(27) Wen, H. M.; Liao, C.; Li, L.; Alsalme, A.; Alothman, Z.; Krishna, R.; Wu, H.; Zhou, W.; Hu, J.; Chen, B. A Metal-Organic Framework with Suitable Pore Size and Dual Functionalities for Highly Efficient Post-Combustion CO_2 Capture. *J. Mater. Chem. A* **2019**, *7*, 3128−3134.

(28) Caskey, S. R.; Wong-Foy, A. G.; Matzger, A. J. Dramatic Tuning of Carbon Dioxide Uptake Via Metal Substitution in a Coordination Polymer with Cylindrical Pores. *J. Am. Chem. Soc.* **2008**, *130*, 10870−10871.

(29) Bao, Z.; Yu, L.; Ren, Q.; Lu, X.; Deng, S. Adsorption of CO_2 and CH_4 on a Magnesium-Based Metal Organic Framework. *J. Colloid Interface Sci.* **2011**, *353*, 549−556.

(30) Kizzie, A. C.; Wong-Foy, A. G.; Matzger, A. J. Effect of Humidity on the Performance of Microporous Coordination Polymers as Adsorbents for CO_2 Capture. *Langmuir* **2011**, *27*, 6368−6373.

(31) McDonald, T. M.; Mason, J. A.; Kong, X.; Bloch, E. D.; Gygi, D.; Dani, A.; Crocellà, V.; Giordanino, F.; Odoh, S. O.; Drisdell, W. S.; Vlaisavljevich, B.; Dzubak, A. L.; Poloni, R.; Schnell, S. K.; Planas,

https://dx.doi.org/10.1021/acs.cgd.0c00202
Cryst. Growth Des. 2020, 20, 3898−3912

N.; Lee, K.; Pascal, T.; Wan, L. F.; Prendergast, D.; Neaton, J. B.; Smit, B.; Kortright, J. B.; Gagliardi, L.; Bordiga, S.; Reimer, J. A.; Long, J. R. Cooperative Insertion of CO_2 in Diamine-Appended Metal-Organic Frameworks. *Nature* **2015**, *519*, 303−308.
(32) Liao, P. Q.; Chen, X. W.; Liu, S. Y.; Li, X. Y.; Xu, Y. T.; Tang, M.; Rui, Z.; Ji, H.; Zhang, J. P.; Chen, X. M. Putting an Ultrahigh Concentration of Amine Groups into a Metal-Organic Framework for CO_2 Capture at Low Pressures. *Chem. Sci.* **2016**, *7*, 6528−6533.
(33) Mulfort, K. L.; Wilson, T. M.; Wasielewski, M. R.; Hupp, J. T. Framework Reduction and Alkali-Metal Doping of a Triply Catenating Metal-Organic Framework Enhances and Then Diminishes H_2 Uptake. *Langmuir* **2009**, *25*, 503−508.
(34) Yang, Q.; Ma, L.; Zhong, C.; An, X.; Liu, D. Enhancement of CO_2/N_2 Mixture Separation Using the Thermodynamic Stepped Behavior of Adsorption in Metal-Organic Frameworks. *J. Phys. Chem. C* **2011**, *115*, 2790−2797.
(35) Xie, L.-h.; Lin, J.-b.; Liu, X.-m.; Wang, Y.; Zhang, W.-x.; Zhang, J.-p.; Chen, X.-m. Porous Coordination Polymer with Flexibility Imparted by Coordinatively Changeable Lithium Ions on the Pore Surface. *Inorg. Chem.* **2010**, *49*, 1158−1165.
(36) Bloch, W. M.; Burgun, A.; Coghlan, C. J.; Lee, R.; Coote, M. L.; Doonan, C. J.; Sumby, C. J. Capturing Snapshots of Post-Synthetic Metallation Chemistry in Metal-Organic Frameworks. *Nat. Chem.* **2014**, *6*, 906−912.
(37) Hu, J.; Liu, Y.; Liu, J.; Gu, C. Computational Screening of Alkali, Alkaline Earth, and Transition Metals Alkoxide-Functionalized Metal-Organic Frameworks for CO_2 Capture. *J. Phys. Chem. C* **2018**, *122*, 19015−19024.
(38) Himsl, D.; Wallacher, D.; Hartmann, M. Improving the Hydrogen-Adsorption Properties of a Hydroxy-Modified MIL-53(Al) Structural Analogue by Lithium Doping. *Angew. Chem., Int. Ed.* **2009**, *48*, 4639−4642.
(39) Mulfort, K. L.; Farha, O. K.; Stern, C. L.; Sarjeant, A. a.; Hupp, J. T. Post-Synthesis Alkoxide Formation Within Metal-Organic Framework Materials: A Strategy for Incorporating Highly Coordinatively Unsaturated Metal Ions. *J. Am. Chem. Soc.* **2009**, *131*, 3866−3868.
(40) Getman, R. B.; Miller, J. H.; Wang, K.; Snurr, R. Q. Metal Alkoxide FunctionalizationinIn Metal-Organic Frameworks for Enhanced Ambient-Temperature Hydrogen Storage. *J. Phys. Chem. C* **2011**, *115*, 2066−2075.
(41) Stergiannakos, T.; Tylianakis, E.; Klontzas, E.; Trikalitis, P. N.; Froudakis, G. E. Hydrogen Storage in Novel Li-Doped Corrole Metal-Organic Frameworks. *J. Phys. Chem. C* **2012**, *116*, 8359−8363.
(42) Han, S. S.; Jung, D. H.; Choi, S. H.; Heo, J. Lithium-Functionalized Metal-Organic Frameworks that Show > 10 wt.% H_2 Uptake at Ambient Temperature. *ChemPhysChem* **2013**, *14*, 2698−2703.
(43) Xiang, Z.; Hu, Z.; Yang, W.; Cao, D. Lithium Doping on Metal-Organic Frameworks for Enhancing H_2 Storage. *Int. J. Hydrogen Energy* **2012**, *37*, 946−950.
(44) Xia, L.; Liu, Q.; Wang, F.; Li, Y. Enhancement Effect of Lithium-Doping Functionalization on Hydrogen Adsorption in Metal-Organic Framework. *Surf. Rev. Lett.* **2017**, *24*, 1750067−1750067.
(45) Wu, D.; Xu, Q.; Liu, D.; Zhong, C. Exceptional CO_2 Capture Capability and Molecular-Level Segregation in a Li-Modified Metal-Organic Framework. *J. Phys. Chem. C* **2010**, *114*, 16611−16617.
(46) Xu, Q.; Liu, D.; Yang, Q.; Zhong, C.; Mi, J. Li-Modified Metal-Organic Frameworks for CO_2/CH_4 Separation: A Route to Achieving High Adsorption Selectivity. *J. Mater. Chem.* **2010**, *20*, 706−714.
(47) Bae, Y. S.; Hauser, B. G.; Farha, O. K.; Hupp, J. T.; Snurr, R. Q. Enhancement of CO_2/CH_4 Selectivity in Metal-Organic Frameworks Containing Lithium Cations. *Microporous Mesoporous Mater.* **2011**, *141*, 231−235.
(48) Babarao, R.; Jiang, J. W. Cation Characterization and CO_2 Capture in Li^+ -Exchanged Metal−Organic FrameworksFrom First-Principles Modeling to Molecular Simulation. *Ind. Eng. Chem. Res.* **2011**, *50*, 62−68.
(49) Cao, Y.; Zhao, Y.; Song, F.; Zhong, Q. Alkali Metal Cation Doping of Metal-Organic Framework for Enhancing Carbon Dioxide Adsorption Capacity. *J. Energy Chem.* **2014**, *23*, 468−474.
(50) Ha, N. T. T.; Lefedova, O. V.; Ha, N. N. Theoretical Study on the Adsorption of Carbon Dioxide on Individual and Alkali-Metal Doped MOF-5s. *Russ. J. Phys. Chem. A* **2016**, *90*, 220−225.
(51) Hu, J.; Liu, J.; Liu, Y.; Yang, X. Improving Carbon Dioxide Storage Capacity of Metal Organic Frameworks by Lithium Alkoxide Functionalization: A Molecular Simulation Study. *J. Phys. Chem. C* **2016**, *120*, 10311−10319.
(52) Kayal, S.; Teo, H. W. B.; Chakraborty, A. Prediction of Phase Transitions by Investigating CO_2 Adsorption on 1% Lithium Doped MIL-101 (Cr) MOF with Anomalous Type Isosteric Heat of Adsorption. *Microporous Mesoporous Mater.* **2016**, *236*, 21−27.
(53) Sokhanvaran, V.; Yeganegi, S. Multiscale Computational Study on the Adsorption and Separation of CO_2/CH_4 and CO_2/H_2 on Li^+-Doped Mixed-Ligand MOF $Zn_2(NDC)_2$(diPyNI). *ChemPhysChem* **2016**, *17*, 4124−4133.
(54) Liu, B.; Zhang, R.; Pan, C. Y.; Jiang, H. L. Unprecedented Li^+ Exchange in an Anionic Metal-Organic Framework: Significantly Enhanced Gas Uptake Capacity. *Inorg. Chem.* **2017**, *56*, 4263−4266.
(55) Cao, Z.; Chen, L.; Jiang, F. L.; Zhou, K.; Yu, M. X.; Jing, T.; Li, S. C.; Li, Z. J.; Hong, M. C. Incorporating Three Chiral Channels into an In-MOF for Excellent Gas Absorption and Preliminary Cu^{2+} Ion Detection. *Cryst. Growth Des.* **2019**, *19*, 3860−3868.
(56) Cui, H.; Ye, Y. X.; Arman, H.; Li, Z. Q.; Alsalme, A.; Lin, R. B.; Chen, B. L. Microporous Copper Isophthalate Framework of mot Topology for C_2H_2/CO_2 Separation. *Cryst. Growth Des.* **2019**, *19*, 5829−5835.
(57) Mu, W.; Liu, D.; Zhong, C. A Computational Study of the Effect of Doping Metals on CO_2/CH_4 Separation in Metal-Organic Frameworks. *Microporous Mesoporous Mater.* **2011**, *143*, 66−72.
(58) Toby, B. H.; Von Dreele, R. B. GSAS-II: The Genesis of a Modern Open-Source All Purpose Crystallography Software Package. *J. Appl. Crystallogr.* **2013**, *46*, 544−549.
(59) Do, D. D. *Adsorption Analysis: Equilibria and Kinetics*; Imperial College Press: London, 1998.
(60) Gasem, K. A. M.; Pan, Z.; Mohammad, S.; Robinson, R. L. Two-Dimensional Equation-of-State Modeling of Adsorption of Coalbed Methane Gases. In *Carbon Dioxide Sequestration in Geological Media: State of the Science*; Grobe, M., Pashin, J. C., Dodge, R. L., Eds.; American Association of Petroleum Geologists: 2010.
(61) Kondo, M.; Okubo, T.; Asami, A.; Noro, S.-i.; Yoshitomi, T.; Kitagawa, S.; Ishii, T.; Matsuzaka, H.; Seki, K. Rational Synthesis of Stable Channel-Like Cavities with Methane Gas Adsorption Properties: [{Cu_2(pzdc)$_2$(L)n}](pzdc = pyrazine-2,3-dicarboxylate;L = a pillar ligand). *Angew. Chem., Int. Ed.* **1999**, *38*, 140−143.
(62) Kondo, M.; Asami, A.; Chang, H.-c.; Kitagawa, S. New Coordination Networks Constructred from N-(4-pyridyl) Isonicotinamide. *Cryst. Eng.* **1999**, *2*, 115−122.
(63) Farrugia, L. J. WinGX and ORTEP for Windows: An update. *J. Appl. Crystallogr.* **2012**, *45*, 849−854.
(64) Bradley, D. C. A Structural Theory for Metal Alkoxide Polymers. *Nature* **1958**, *182*, 1211−1214.
(65) Chisholm, M. H.; Drake, S. R.; Naiini, A. A.; Streib, W. E. The Synthesis and Characterization of Volatile Lithium Alkoxides, and the Single Crystal X-Ray Structure of $[LiOCMe_2Ph]_6$. *Polyhedron* **1991**, *10*, 805−810.
(66) Nekola, H.; Olbrich, F.; Behrens, U. Crystal and Molecular Structures of Lithium and Sodium Tert-Butoxide. *Z. Anorg. Allg. Chem.* **2002**, *628*, 2067−2070.
(67) Allan, J. F.; Nassar, R.; Specht, E.; Beatty, A.; Calin, N.; Henderson, K. W. Characterization of a Kinetically Stable, Highly Ordered, Octameric Form of Lithium Tert-Butoxide and Its Implications Regarding Aggregate Formation. *J. Am. Chem. Soc.* **2004**, *126*, 484−485.
(68) Hamalainen, J.; Holopainen, J.; Munnik, F.; Hatanpaa, T.; Heikkila, M.; Ritala, M.; Leskela, M. Lithium Phosphate Thin Films

https://dx.doi.org/10.1021/acs.cgd.0c00202
Cryst. Growth Des. 2020, 20, 3898−3912

Grown by Atomic Layer Deposition. *J. Electrochem. Soc.* **2012**, *159*, A259−A263.
(69) Markowitz, M. M.; Boryta, D. A. Lithium Metal-Gas Reactions. *J. Chem. Eng. Data* **1962**, *7*, 586−591.
(70) McFarlane, E. F.; Tompkins, F. C. Nitridation of Lithium. *Trans. Faraday Soc.* **1962**, *58*, 997−1007.
(71) McHale, J. M.; Navrotsky, A.; Kowach, G. R.; Balbarin, V. E.; DiSalvo, F. J. Energetics of Ternary Nitrides: Li-Ca-Zn-N and Ca-Ta-N Systems. *Chem. Mater.* **1997**, *9*, 1538−1546.
(72) Schiemann, M.; Fischer, P.; Bergthorson, J.; Schmid, G.; Taroata, D. Combustion of Lithium Particles in N_2—Reaction Rates. *Combust. Sci. Technol.* **2017**, *189*, 169−186.
(73) Danzer, G. D.; Golus, J. A.; Strommen, D. P.; Kincaid, J. R. Resonance Raman Spectra and Normal Modes of Vibration of 2,2′-Bipyridine Anion Radicals. *J. Raman Spectrosc.* **1990**, *21*, 3−8.
(74) Topaçli, A.; Akyüz, S. 4,4′-Bipyridyl: Vibrational Assignments and Force Field. *Spectrochim. Acta, Part A* **1995**, *51*, 633−641.
(75) Shurvell, H. F.; Southby, M. C. Infrared and Raman Spectra of Tetrahydrofuran Hydroperoxide. *Vib. Spectrosc.* **1997**, *15*, 137−146.
(76) Zhuang, Z.; Cheng, J.; Wang, X.; Zhao, B.; Han, X.; Luo, Y. Surface-Enhanced Raman Spectroscopy and Density Functional Theory Study on 4,4′-Bipyridine Molecule. *Spectrochim. Acta, Part A* **2007**, *67*, 509−516.
(77) Sayin, E.; Kürkçüotlu, G. S.; Yeşilel, O. Z.; Hökelek, T. Syntheses, Crystal Structures and Spectroscopic Properties of Copper(II)-Tetracyanometallate(II) Complexes with Nicotinamide and Isonicotinamide Ligands. *J. Mol. Struct.* **2015**, *1096*, 84−93.
(78) Bhat, S. A.; Faizan, M.; Alam, M. J.; Ahmad, S. Vibrational and Electronic Spectral Analysis of 2,3-Pyrazinedicarboxylic Acid: A Combined Experimental and Theoretical Study. *Spectrosc. Lett.* **2016**, *49*, 449−457.
(79) Kumari, G.; Patil, N. R.; Bhadram, V. S.; Haldar, R.; Bonakala, S.; Maji, T. K.; Narayana, C. Understanding Guest and Pressure-Induced Porosity Through Structural Transition in Flexible Interpenetrated MOF by Raman Spectroscopy. *J. Raman Spectrosc.* **2016**, *47*, 149−155.
(80) Świderski, G.; Lewandowska, H.; Świsłocka, R.; Wojtulewski, S.; Siergiejczyk, L.; Wilczewska, A. Thermal, Spectroscopic (IR, Raman, NMR) and theoretical (DFT) Studies of Alkali Metal Complexes with Pyrazinecarboxylate and 2,3-Pyrazinedicarboxylate Ligands. *J. Therm. Anal. Calorim.* **2016**, *126*, 205−224.
(81) Stepakova, L. V.; Skripkin, M. Y.; Chernykh, L. V.; Starova, G. L.; Hajba, L.; Mink, J.; Sandstrom, M. Vibrational Spectroscopic and Force Field Studies Of Copper(II) Chloride and Bromide Compounds, and Crystal Structure of $KCuBr_3$. *J. Raman Spectrosc.* **2008**, *39*, 16−31.

https://dx.doi.org/10.1021/acs.cgd.0c00202
Cryst. Growth Des. 2020, 20, 3898−3912